SELENOLOGY TODAY 25

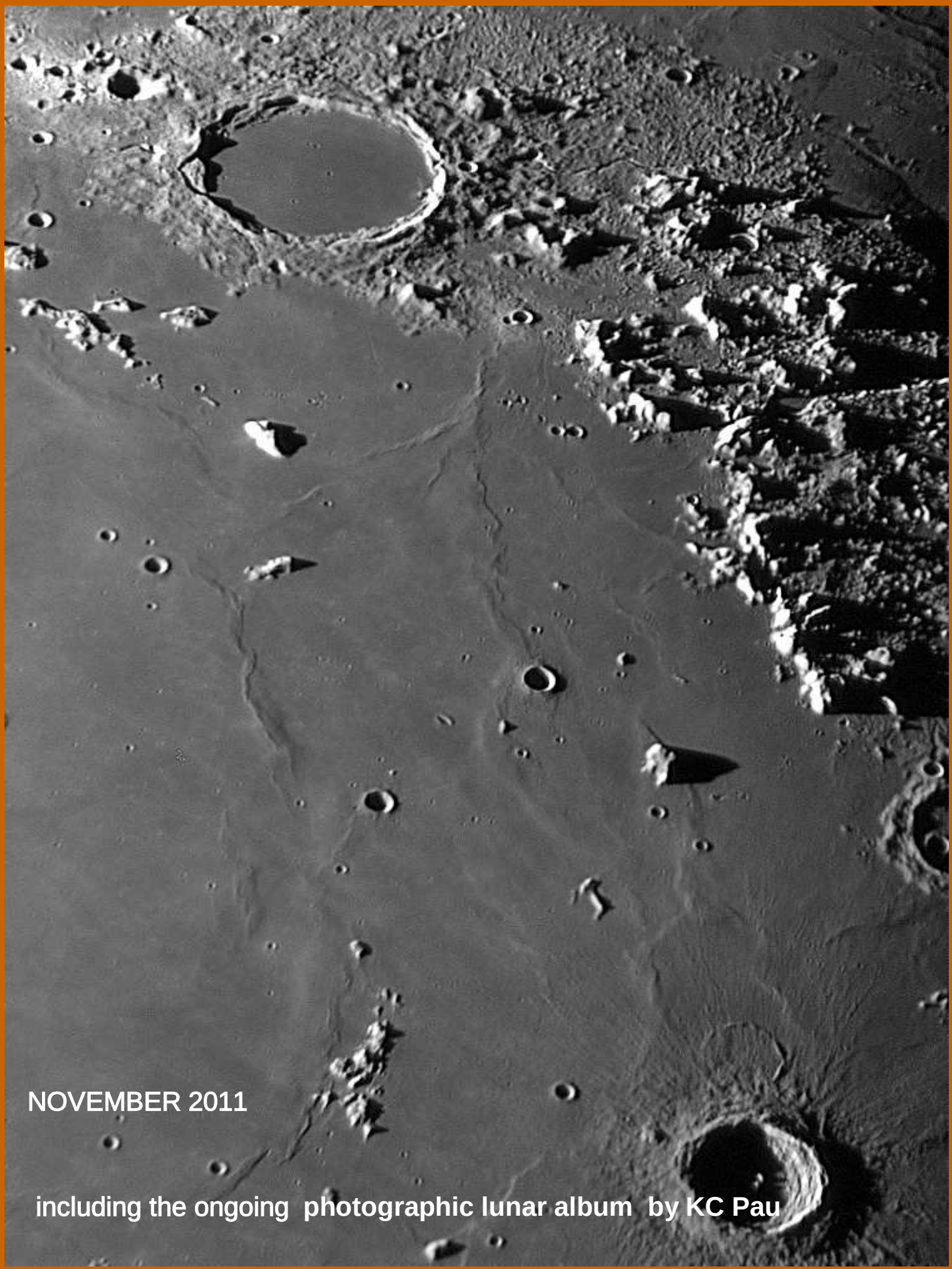

NOVEMBER 2011

including the ongoing photographic lunar album by KC Pau

GLR GROUP.org
Geological Lunar Researches Group

Selenology Today **is devoted to the publication of contributions in the field of lunar studies. Manuscripts reporting the results of new research concerning the astronomy, geology, physics, chemistry and other scientific aspects of Earth's Moon are welcome.**

Selenology Today **publishes papers devoted exclusively to the Moon. Reviews, historical papers and manuscripts describing observing or spacecraft instrumentation are considered.**

The Selenology Today

Editorial Office

selenology_today@christian-woehler.de

Cover

KC PAU

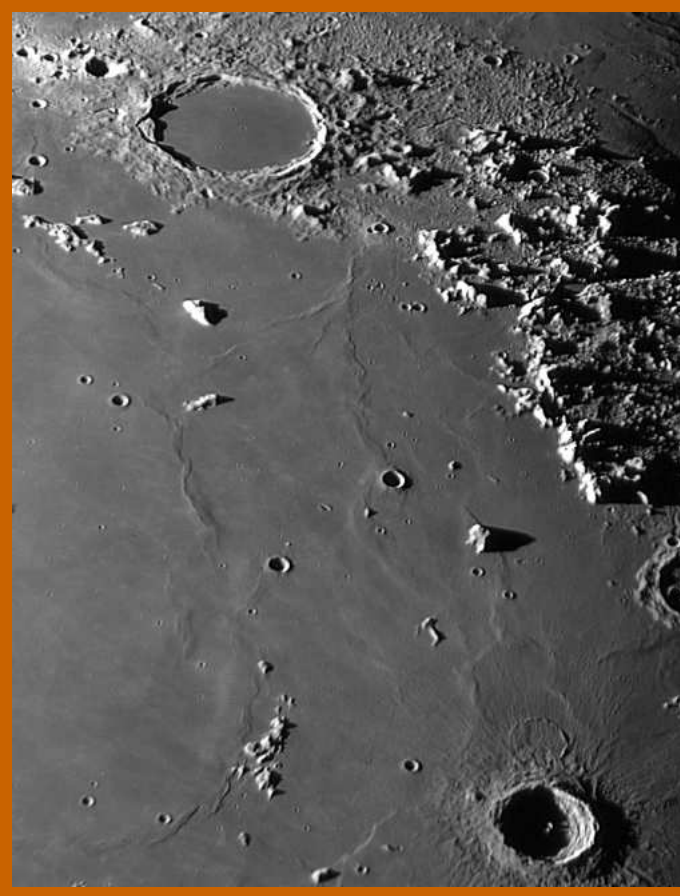

Selenology Issue 25 November 2011

SELENOLOGY TODAY #25

November 2011

Selenology Today website

http://digilander.libero.it/glrgroup/

Humboldt: Concentric Crater and LPDs

by H. Eskildsen [(a)] and R. Lena [(b)]

(a) Association of Lunar and Planetary Observers, American Lunar Society, Alachua Astronomy Club

(b) Geologic Lunar Research (GLR) group

Abstract: *The concentric crater in Humboldt falls in the typical range of diameter and ratio of inner to outer ring (Di/Do) for concentrics. The proximity of two much younger, non-concentric, craters similar in size to the concentric crater suggests that conditions causing the concentric crater formation no longer existed at the time of their impact. Albedo observations and spectral studies indicate that its interior is composed of highland type material and not of volcanic extrusions. These observations support the hypothesis of formation of concentric craters by igneous intrusion rather than by volcanic extrusion.*

Humboldt Concentric Crater

Near the eastern margin of the floor of the large, floor-fractured crater, Humboldt, lies a small, 8.9 km concentric crater at approximately 83.35° east, 26.55° south. The concentric crater rests 14 km south of the lunar pyroclastic deposit (LPD) on the northeastern margin of Humboldt. Two other much younger, small craters rest within 14 km of the concentric crater. The larger to the east, labeled “a”, is approximately 9.6 km in diameter and is centered at 26.60° S, 83.78° E, and the smaller crater to the southwest, labeled “b”, is approximately 6.5 km in diameter centered at 26.94° S, 83.16° E. Position measurements were taken directly from mouse position readings of the online LROC WMS Image Map (http://wms.lroc.asu.edu/lroc#damoon), and diameters were determined by establishing the number of km per pixel from the LROC scale on the image, measuring crater pixel diameters and then multiplying by the number of km per pixel (cf. Table 1).

Figure 1 is oriented with east up and north to the left and plainly shows Humboldt, Humboldt N, the northeastern LPD, and craterlets a and b. The concentric crater is not readily visible on this high sun angle image, but lies just below (to the west) of craterlet a. "P" denotes the central peak.

Figure 2 shows the features noted above, and the concentric crater is plainly visible in the low sun angle image, but it does not appear concentric on this image due to its location close to the limb.

Clementine images show the rims and floor of the concentric crater to have been smoothed and softened by space weathering (cf. Fig. 3). The two other nearby craters have sharp rims with bright interiors and are much younger. On the telescope image with high sun illumination both of the younger craters are visible due to higher albedo than the surroundings, while the concentric crater albedo matches and blends in to the background and cannot be distinguished. Other images at lower sun angles plainly show the presence of the concentric crater, though not necessarily its inner ring. It is possible that under favorable librations, the inner concentric crater would be visible through modest-sized telescopes.

Figure 4 shows the LROC WMS Image Map Calibration for crater diameter measurements.

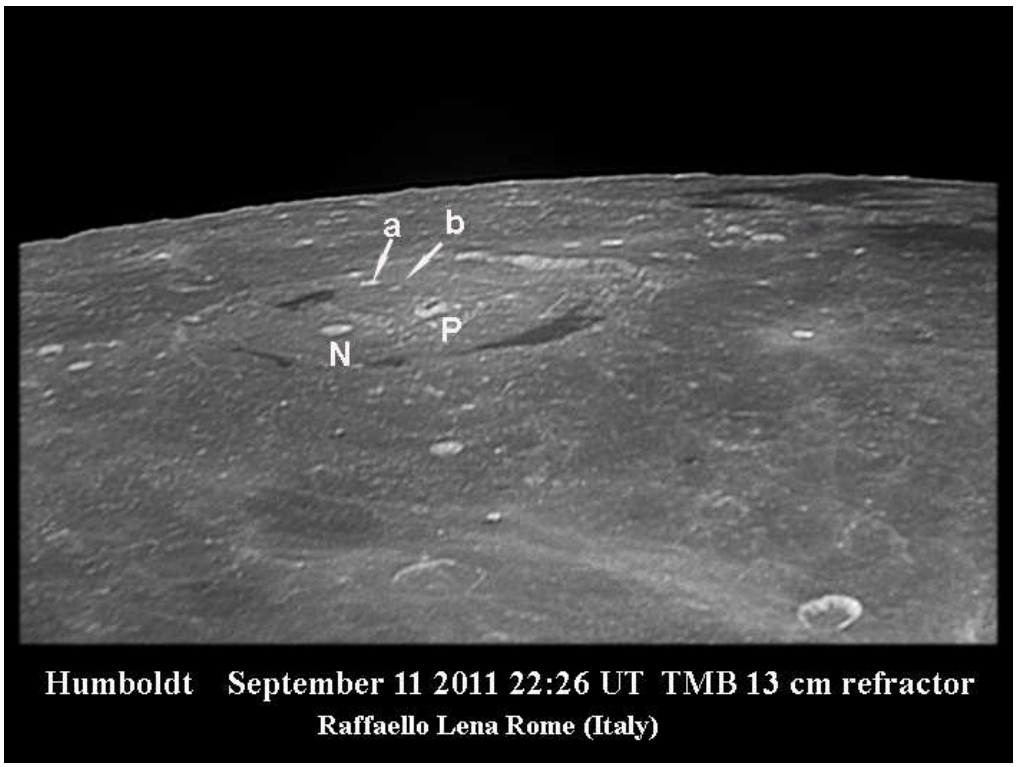

Figure 1. Humboldt region. Image made by R. Lena (see text for detail).

Figure 2. Humboldt region. Image made by H. Eskildsen (see text for detail).

	Pixels	Measured Diameter
Humboldt N	126	15.1 km (LICD V9Feb2009 lists 14 km—8% error)
Humboldt CC	74	8.9 km (0.12 km/pixel)
Humboldt CC Inner ring	42	5.0 km (0.12 km/pixel)
Humboldt a	80	9.6 km (0.12 km/pixel)
Humboldt b	54	6.5 km (0.12 km/pixel)

Table 1

The Humboldt concentric crater (Hcc) is typical of an average concentric crater based on reports by C.A. Wood in 1978, and Trang et al. in 2011. Its morphology is similar to the larger concentric Hesiodus A, as are 70% of the 58 known concentric craters, and both appear to be of similar age. Concentric craters range from three to 20 km in diameter, and the Hcc diameter of 8.9 km is very close to the median of 8 km. Its ratio of the inner ring diameter to the outer ring diameter (Di/Do ratio) is 0.56, compared to the median ratio around 0.5. Most concentric craters are located in areas that show evidence of volcanic intrusive and extrusive activity such as mare margins or floor-fractured craters. Hcc is located on the near the margin of a floor-fractured crater not far from a lunar pyroclastics deposit.

The close proximity of two normal craters of similar size but different ages from the concentric crater within the floor-fractured crater Humbolt gives clues as to the origin of the concentric craters. It would seem likely that if impact into a layered target were the cause, all three craters would be concentric. Of the several remaining hypotheses proposed for the formation of concentric craters, only two further possibilities are viable given the limited distribution of concentric craters, volcanic extrusion and igneous intrusion (Trang et al., 2011).

The volcanic extrusion hypothesis suggests that after crater formation, lava penetrated through the floor to create a ring of volcanic rock that would be different from the original impacted formation. The igneous intrusion hypothesis proposes that magma intruded into the layers below the concentric crater, distorting it to form the inner ring. In this case no magma reached the surface and therefore the floor, walls and surrounding area would be of the same material.

The floor of Humboldt obviously experienced magma intrusion to raise, distort and crack the crater floor, and igneous extrusion in the form or pyroclastics that are visible within 15-20 km of all three craters. The dark pyroclastics contrast sharply with the medium albedo crater floor and interior of the concentric crater, while the immature soils inside the two other craters are brighter still. Since the younger craters are not concentric, it is quite likely that by the time of their impacts, the magma had solidified, and intrusion and extrusion had ceased altogether. Furthermore, the estimated depth of excavation of the younger craters can be used to set an upper limit of the depth of the intrusive magma.

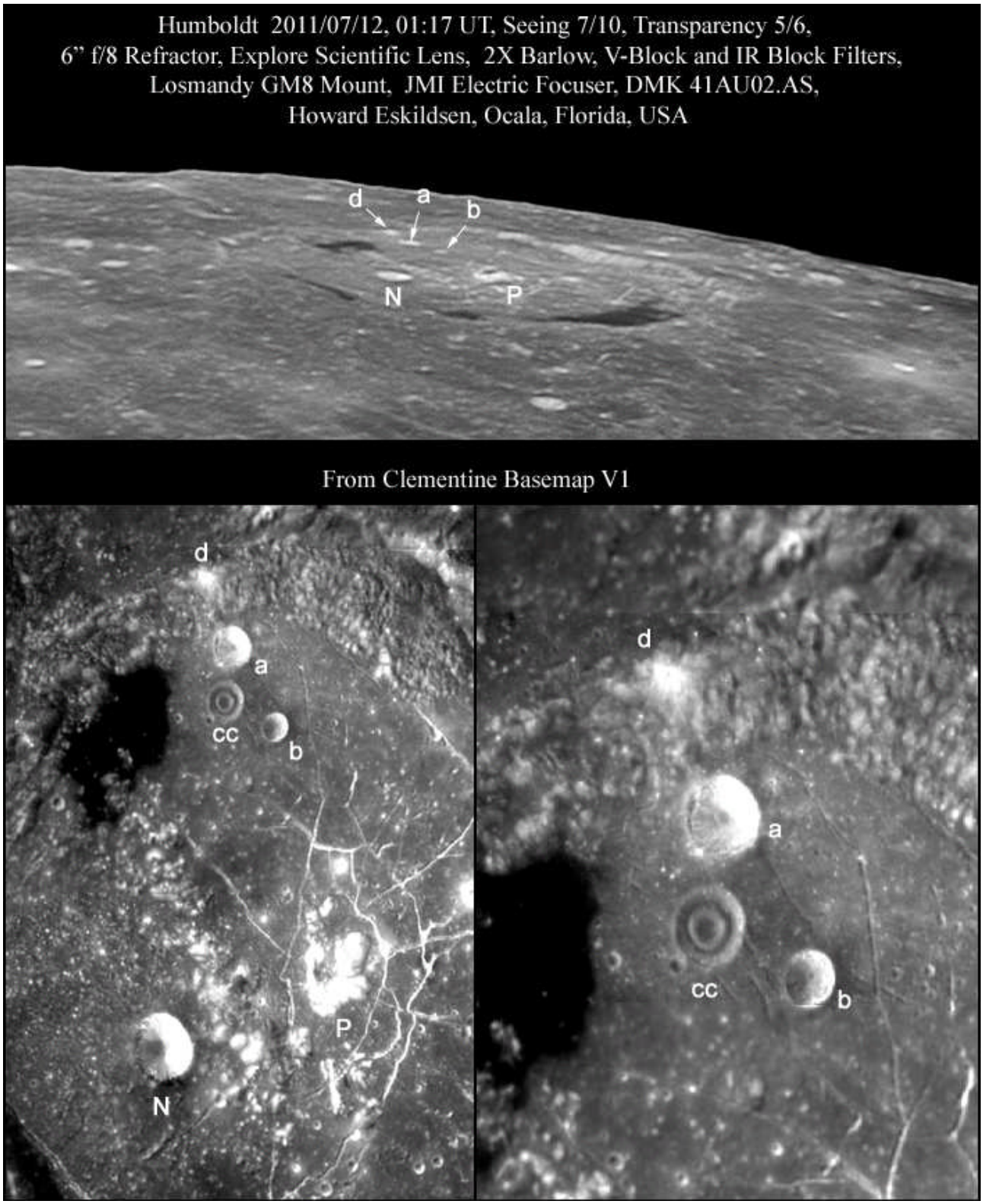

Figure 3. Humboldt region. Image made by H. Eskildsen and Clementine imagery (see text for detail).

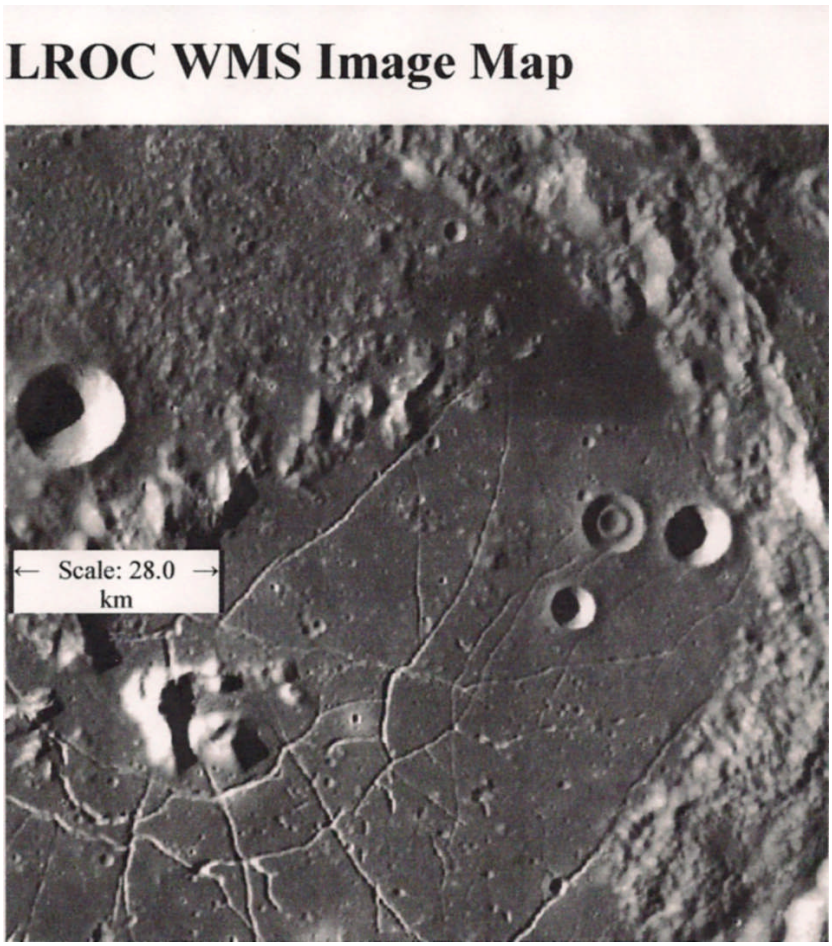

Figure 4. LROC WMS Image Map Calibration for crater diameter measurements (cf. Table 1).

The intrusive material beneath the area of the craters under study must be deeper than the excavation depth of the craters; otherwise the crater interiors should show different albedo and composition from the surrounding surface material. In the doctoral thesis by Irene Antonenko, experiments with hypervelocity projectiles suggested that the thickness of material overlying darker (mafic) maria can be expressed by the equation:

$t(m) = 0.066*D(r)$ with an error of ± 15%, where t(m) is the thickness of the bright overlying layer and D(r) = the rim diameter of the smallest crater that could produce a dark halo.

This equation is for simple craters under 19 km in diameter. Since none of the craters around Hcc show any hint of interior compositional difference or dark halo, the intrusive material must be deeper.

For the 9.6 km crater labeled “a” the mafic intrusive must be more than 0.63 km below the surface, since the interior of the crater is of similar composition to the surrounding terrain.

The absence of a dark halo around Humboldt N suggests that the intrusive material must be at least 1 km below the surface in that region.

Visual observation studies give clues to the formation of concentric crater formation, however, to further differentiate between intrusion and extrusion requires spectral analysis of the composition of the different areas. As can be seen from the high sun angle photos, the albedo of the concentric crater matches the albedo of its immediate surroundings which would support the intrusion hypothesis. Spectral analysis is even more revealing than simple observational albedo comparison.

Spectral analysis of Humboldt

This analysis employs the Clementine UVVIS+NIR spectral mapping technique developed by Evans et al. (2009a; 2009b). The technique is used to produce spectral maps of the principal spectral mafic absorption features for lunar terrain of interest (Fig. 5). It was employed here in an attempt to discern the mineralogy of the examined region. The spectral mapping was obtained using the implementation in Octave as described by Evans and Lena (2010). The 5 UVVIS (415, 750, 900, 950, and 1000 nm) and 4 NIR wavelengths (1100, 1250, 1500, 2000 nm) are available at the PDS Map-a-Planet site (http://www.mapaplanet.org/explorer/moon.html). The spectral data resulted in the automated production of maps concerning:

a) band center minimum

b) band depth

c) FWHM (full height at half maximum).

The spectra were then represented as continuum divided UVVIS+NIR spectra (Fig. 6). The continuum division by the line between the 750 nm and the 1500 nm reflectance value was used.

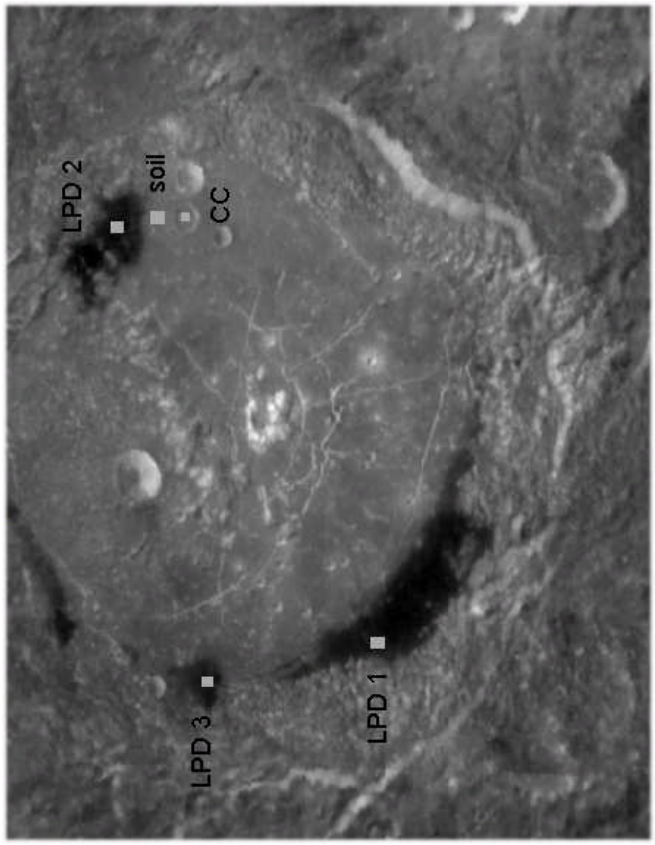

Figure 5. Clementine 750 nm image with the examined features.

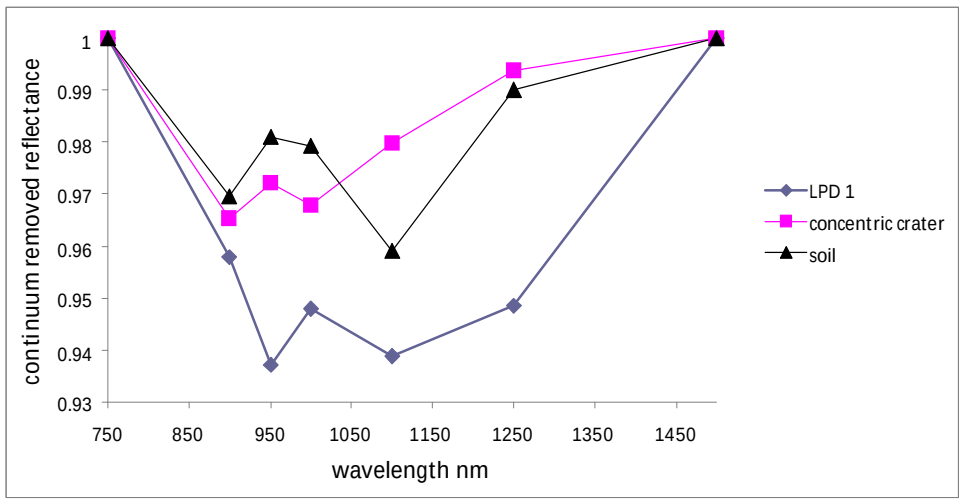

Figure 6. Spectra of the LPD1, concentric crater and nearby soil.

The greater the amount of iron present, the greater the band depth and the more mafic the terrain is. Amounts of iron under about 5% are not very mafic and are typically anorthositic. Such terrain constitutes the majority of the lunar highlands. Noritic features usually have band centers under 950 nm and band depths significantly greater than 5%. FWHM band width is usually significantly less than 300 nm. In contrast, high calcium content pyroxenes are called clinopyroxenes. Small amounts of clinopyroxenes, typically less than 5%, are found in the rather anorthositic soils of the lunar highlands. More mafic clinopyrene content is found in mare basalts. Clinopyroxenes show band centers between 950 nm and 1000 nm. Their FWHM widths are similar to those of orthopyroxenes. Olivine has a band center above 1000 nm. Some lunar mare also contain significant amounts of olivine. The FWHM width of olivine is wider than that of orthopyroxene or clinopyroxene and is usually greater than 300 nm.

Examination of spectral maps reveals that the region of LPDs are composed of admixed quantity of clinopyroxene and olivine (Fig. 6). The average FWHM band width for the pyroclastic deposit 1 is about 390 nm ± 30 nm with a trough depth of about 6 to 7%. This is significantly more than the band width for the adjacent soil and the concentric crater with a band center wavelength of about 900 nm. The concentric crater has band depth and FWHM values of 3.5-4.4% and 260-340 nm, respectively, while the soil displays band depth of 3.6-4.4 % and FWHM of 360 nm. This finding could be consistent with the presence of an additional component consisting of clinopyroxene, olivine or a mixture of these.

The interpretation is confirmed using the segregated maps corresponding for orthopyroxene band center (890 to 945 nm), clinopyroxene band center (950 to 1000 nm), and olivine band centers (1005 to 1100 nm). The segregated maps are then used to derive a false color map where the red channel is assigned to orthopyroxene, green channel to olivine and blue channel to clinopyroxene (Fig. 7).

Calculation of Elemental Abundances using Clementine UVVIS+NIR data

Lunar Prospector (LP) data provides elemental abundance ground truth, but at low spatial resolution. This resolution, however, may be increased using the method described by Wöhler et al. (2009; 2011) which represents LP data in terms of a transformation of spectral parameter maps for the absorption trough near 1000 nm derived from Clementine UVVIS+NIR imagery.

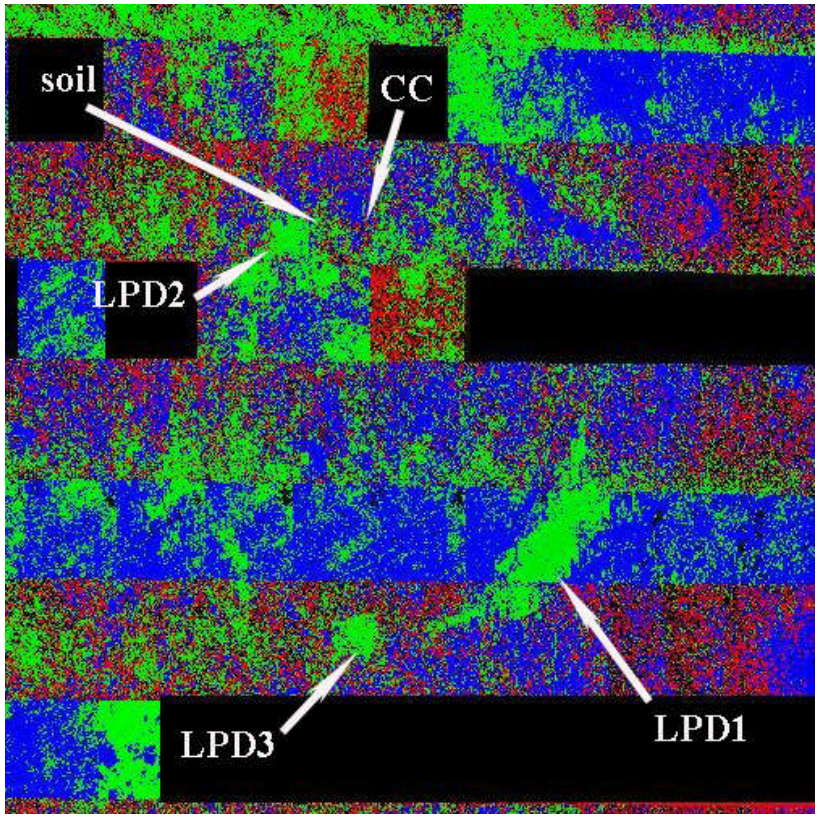

Figure 7. Segregated maps used to derive a false color map where the red channel is assigned to orthopyroxene, green channel to olivine and blue channel to clinopyroxene.

Creation of these spectral maps is discussed in Evans et al. (2009a). For more details about this technique refer to Wöhler et al. (2011). Mathematically, a data matrix can be represented by the transformation of a second matrix according to equation (1) where matrix x and matrix b are of the same width:

$$Ax = b \qquad (1)$$

Using this model, the global LP elemental abundance map for a given element is termed the ground truth matrix and is matrix b. It is a row matrix of height one and width equal to the row*column dimension of the LP image.

A set of spectral parameter maps includes the band center, band depth, FWHM and slope, where only the deepest minimum is regarded, and their quadratic combinations. Each row in matrix x consists of one of these spectral maps written as a single row

matrix of height one and width equal to the row*column dimension of the map image. In addition to the spectral maps described above, their pairwise product maps are also added to matrix x.

Matrix A is the coefficient matrix giving the gain and offset values that matrix b must be applied to effect its transformation into a form approximate to matrix x.

When the equation Ax = b is solved for A using standard linear algebra techniques, one obtains the gain and offset coefficients necessary to transform matrix x into an approximation of the ground truth matrix b.

Matrix A has height one and width equal to the number of rows in matrix x. The last element in Matrix A is the offset and all other elements are gain coefficients. This feature set does not comprise the albedo itself, and produces a similarly good fit to the global LP data as the Lucey Fe and Ti abundances (Lucey et al., 2000).

These gain and offset coefficients, once derived, are also applicable to any other set of Clementine based spectral maps even though they represent a much higher spatial resolution than the global maps used to determine the coefficients.

The uncertainty of the derived elemental abundance maps is ± 1 wt%. Based on this approach, the abundances of the elements Ca, Al, Fe, Mg, Ti, and O were estimated (Fig. 8).

The wt % range is as follows: aluminum (0-20 wt %), calcium (2-18 wt %), iron (0-25 wt %), magnesium (0-16 wt %), oxygen (40-47 wt %), and titanium (0-6 wt %).

As an aid to interpreting the composition, the elemental abundances in wt% for each pixel block (see Fig. 5) were assessed and are shown in Table 2.

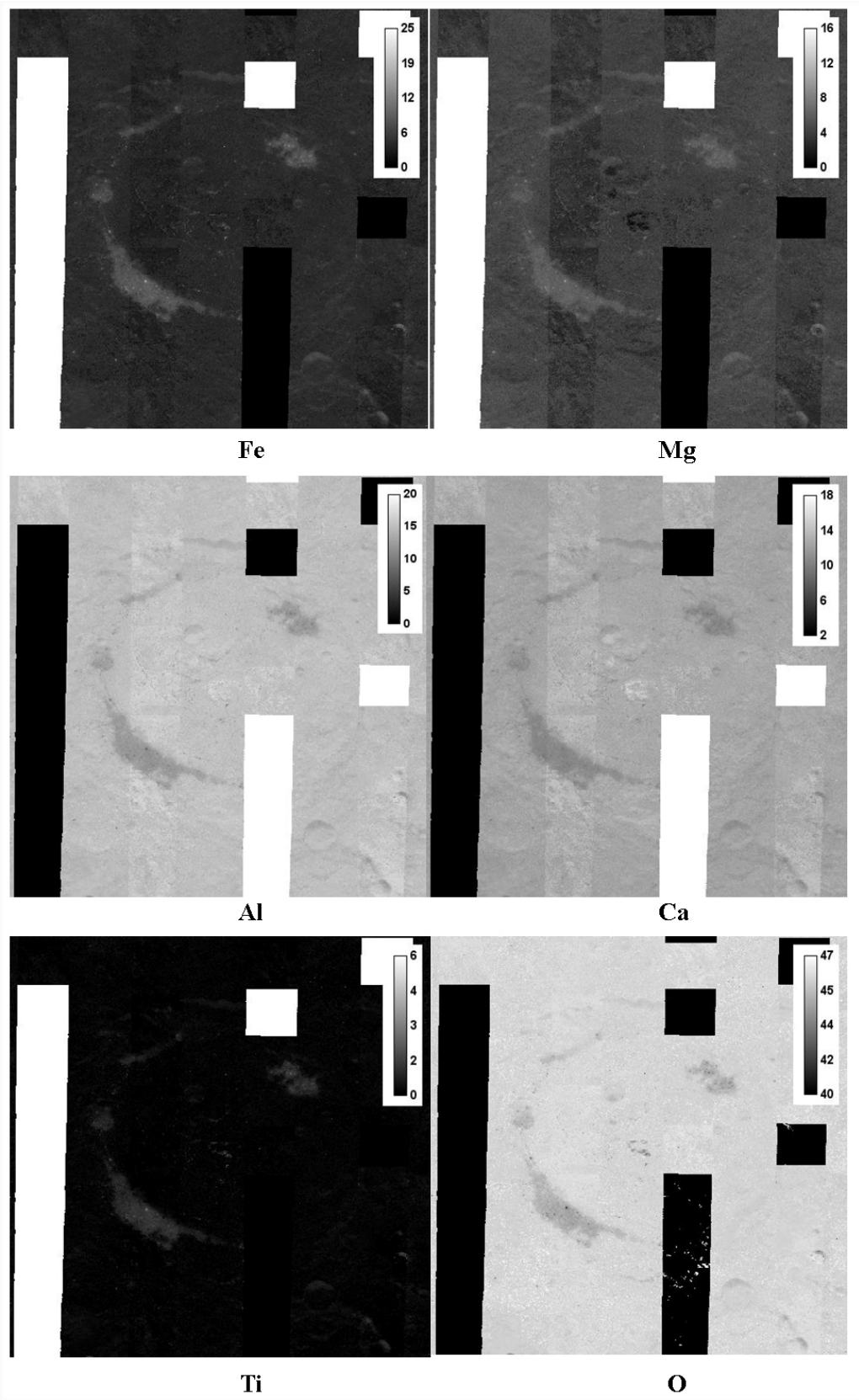

Figure 4. Elemental analysis.

The higher values for Fe and Ti were inferred at LPDs, with 7.6-8.5 wt% Fe, 0.9-1.06 wt% Ti, and 5.6-6.3 wt% Mg. The lower values for Fe (< 4.5 wt%), Mg (< 4.2 wt%) and Ti (<0.2 wt %) correspond to higher amounts of Aluminum and Calcium wt%, inferred for the concentric crater and the nearby soil, typical of highland composition (cf. Table 2).

The Mg/Al ratio is less than 1.0 and would not be consistent with a volcanic glass in the examined LPDs. Most volcanic glasses have Mg/Al ratios in the range of 1.7 to 3.3.

	LPD 1 wt%	LPD 2 wt%	LPD 3 wt%	CC wt%	soil wt%
Fe	8.3	8.5	7.6	4.4	4.0
Mg	6.3	6.2	5.6	4.1	4.0
Al	11.7	11.9	12.6	14.9	15.2
Ca	10.3	10.4	10.9	12.4	12.4
Ti	1.06	1.0	0.9	0.1	0.1
O	45.0	44.7	45.1	45.9	46.0

Table 2

Petrographic maps

The topographic distribution of rock types can be derived from elemental abundance maps using the three end-member model described by Berezhnoy et al. (2005). The petrographic maps shown in Fig. 5 indicate the relative fractions of the three end-members mare basalt (red channel), Mg-rich rock (green channel), and ferroan anorthosite (FAN, blue channel). Another petrographic map, termed petrographic basalt map, was then represented as relative fractions of the three end-members: Red for mare basalt with low Titanium amounts (Al 9 wt%, Ti 1.5 wt%), Green for highland-like material (Al 14 wt%, Ti 0.5 wt%) and Blue for titanium rich basalt (Al 6.3 wt%, Ti 3.6 wt%).

In this map regions appearing in green are composed of highland material (or sometime mare basalt contaminated with highland material by lateral mixing effects). Only the LPDs are of basaltic composition where the craters (including the concentric crater) are of highland composition. Pyroclastic deposits have been recognized all across the Moon, identified by their low albedo, smooth texture, and mantling relationship to

underlying features (Gaddis et al., 2003). According to Gaddis et al. (2003) we have studied Humboldt dark deposits. Spectral properties suggests that at least some portion of these materials may be ponded lavas rather than pyroclastic material. Hence this region has undergone an intrusion process (floor-fractured crater) and a subsequent explosive phase of volcanism.

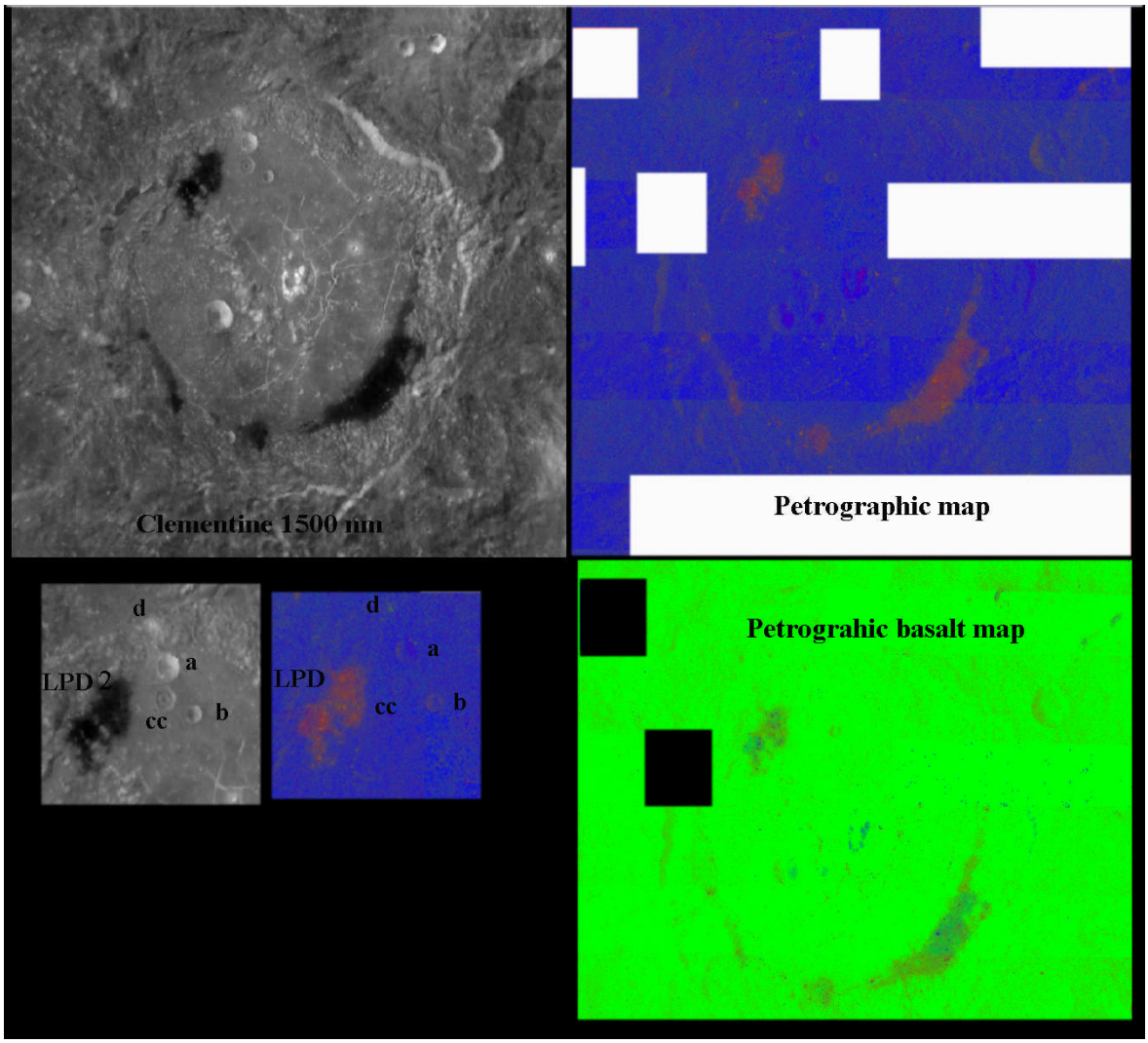

Figure 5. Petrographic maps.

Humboldt is a floor-fractured craters differing from concentric craters morphologically, as most floor-fractured craters do not contain an inner ring. Interpretations for the origin of concentric craters and their inner torus include exogenic and endogenic processes, including volcanic extrusion and igneous intrusion as mechanism (cf. Trang et al., 2011). Using the derived elemental abundance maps no compositional differences between the interior of concentric crater and the surrounding area is observed. The lack of this compositional difference between concentric craters and the surrounding area suggests mafic extrusion is not a likely scenario and intrusion could be the most likely candidate in forming concentric crater in Humboldt taking into account the mechanism argued by Trang et al. (2011).

Conclusion

Three similar sized craters lie in proximity on the western floor of the crater Humboldt, only one of which is a concentric crater. The other craters are notably younger than the concentric, suggesting that processes responsible for the concentric may have ceased by the time of the latter impacts. Albedo observations reveal the concentric crater to be of same brightness as the surrounding terrain which is notably brighter than the dark lunar pyroclastics (LPD) deposits to the north. Spectral analysis shows the interiors of the concentric crater and the other two craters to be of highland material, without exposed mafic material. The mafic intrusion that elevated the floor of Humboldt and caused the LPD to the north must be deeper than 0.63 km by non-concentric crater “a”. These visual and spectral findings support the igneous intrusion hypothesis of formation of concentric craters.

References

[1] Antonenko, I., Cintala, M.J. and Hšrz, F., 1999. Experimental Studies of Dark-Haloed Craters: Implications for the Thickness Measurements of Lunar Cryptomafic Deposits, Department of Geological Sciences, Brown University, Providence, RI, USA.

See: http://clients.teksavvy.com/~iant/Thesis/

[2] Berezhnoy, A.A. , Hasebe, N., Kobayashi, M., Michael, G. G., Okudaira, O., Yamashita, N. A. 2005. Three end-member model for petrologic analysis of lunar prospector gamma-ray spectrometer data. Planetary and Space Science, Volume 53, 11, 1097-1108.

[3] Evans, R., Wöhler, C., Lena, R., 2009a.Analysis of Absorption Trough Features Using Clementine UVVIS+NIR Imagery. *Lunar Planetary Science Conference*, XXXX, abstract #1093.

[4] Evans, R., Wöhler, C., and Lena, R., 2009b. Spectral mapping using Clementine UV-Visible-NIR Data Sets: Applications to Lunar Geologic Studies. Selenology Today, Vol. 14 pp. 1-70.

[5] Evans, R. and Lena, R., 2010. Short Octave Program to Map Lunar Spectral Features: Application to Lunar Geologic Studies. Selenology Today, 18, 1-19.

[6] Gaddis, L.R., Staid, M.I., Tyburczy, J.A., Hawke, B.R., Petro, N.E., 2003. Compositional analyses of lunar pyroclastic deposits. Icarus 161, 262–280.

[7] Lucey, P. G., Blewett, D. T., Jolliff, B.L., 2000. Lunar iron and titanium abundance algorithms based on final processing of Clementine ultraviolet-visible images, J. Geophys. Res., 105(E8), 20, 297–20,305.

[8] Trang D., Gillis-Davis J., Hawke B., Bussy D., 2011 The Origin of Lunar Concentric Craters, *42nd Lunar and Planetary Science Conference*, 1698.

[9] Wöhler, C., Berezhnoy, A., Evans, R., 2009. Estimation of Lunar Elemental Abundances Using Clementine UVVIS+NIR Data. Proc. European Planetary Science Congress, EPSC2009-263.

[10]Wöhler, C., Berezhnoy, A., Evans, R., 2011. Estimation of Elemental Abundances of the Lunar Regolith Using Clementine UVVIS+NIR Data. Planetary and Space Science, vol. 59, no. 1, pp. 92-110.

[11] Wood C.A., 1978. Lunar Concentric Craters, *Lunar Planetary Science Conference IX*, 1264-1266.

A photographic lunar album

by KC Pau

Geologic Lunar Research (GLR) group

Introduction

Dear readers,

I am now preparing a photographic lunar album from the archive of the lunar images that I have taken in these few years. The aim of this album does not serve as a lunar atlas, though it covers almost the whole surface of the near side Moon. I may say the album is a collection of my best quality lunar images to share among the observers in the lunar world.

The content of the album is mainly composed of wide field lunar images of certain regions of the Moon under different illumination, if available. The scale of the images is approximately the same as that of the the Rukl's atlas. High resolution images of certain features are supplemented. The wide-field images are arranged from east to west, and then from south to north to cover the whole surface of the moon if possible. Orientation is south up and east to the left as view in a Newtonian reflector. As this is a photographic album, text will be kept to a minimum as the information about the features is fully discussed in other media.

The last part of the album is the mosaic of certain lunar regions to cover a wider area than that of the wide-field images.

I must thank Raffaello Lena of the GLR group to give me chance to publish some sample pages in Selenology Today. Thank you all to spare time to read these sample pages. Your valuable comment about the format and content of this album is anticipated to make it more perfect.

My email address is: kcpaulhk@yahoo.com.hk

KC Pau

Front cover of the album

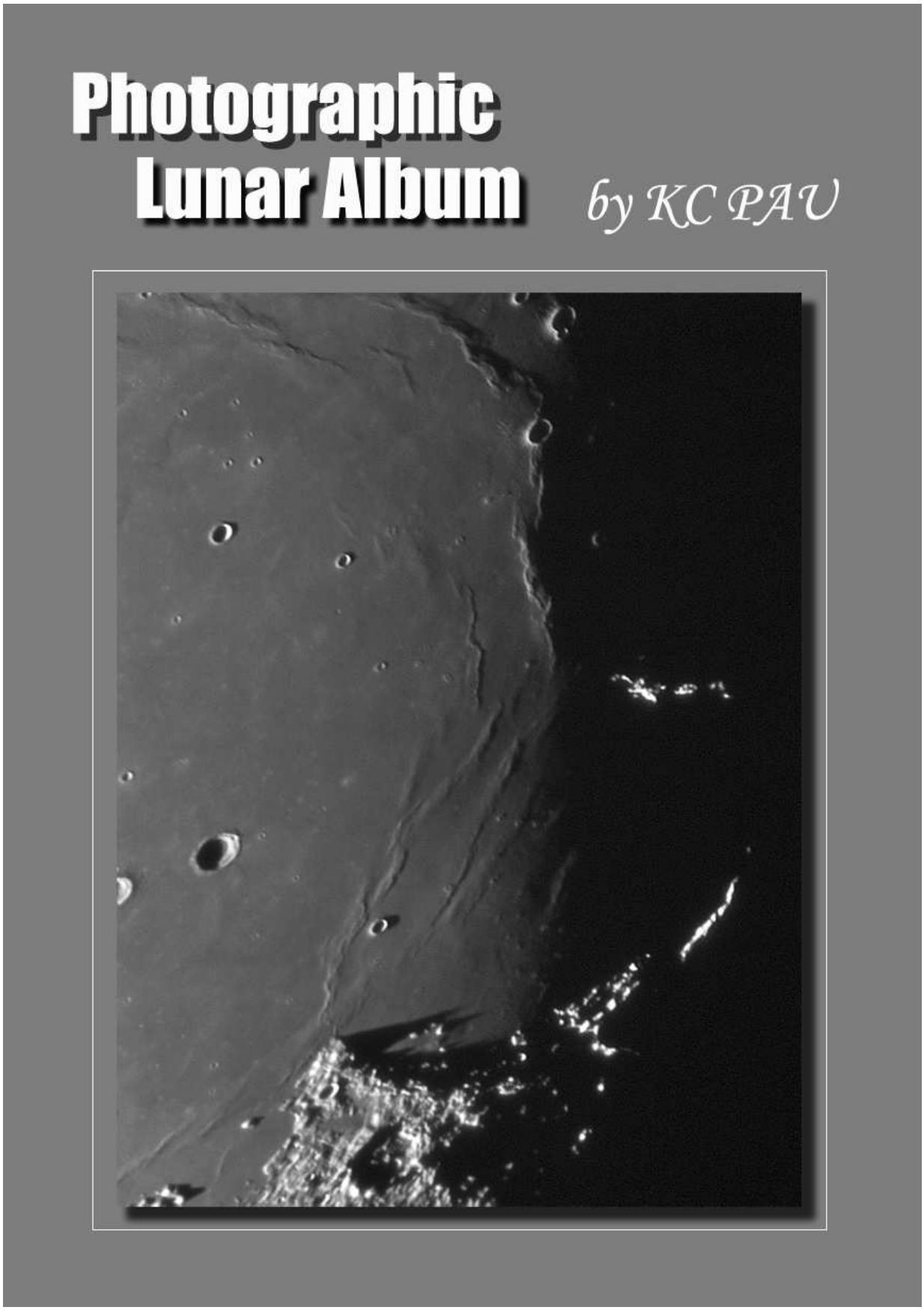

Eratosthenes and its vicinity

-----Text to be prepared-----

There are many domes around Eratosthenes region. Geological Lunar Researches Group had a detail study of the four of the many domes here. It is concluded in their report that "None of these domes in the Eratothenes region seem to have a summit pit, so it is likely that subsurface magmas have swelled, but not punctured the lunar surface." More information about this study is obtained from their website or from Selenology, the Journal of the American Lunar Society, Vol. 23 No. 4. These four domes are indicated in Fig. 5.

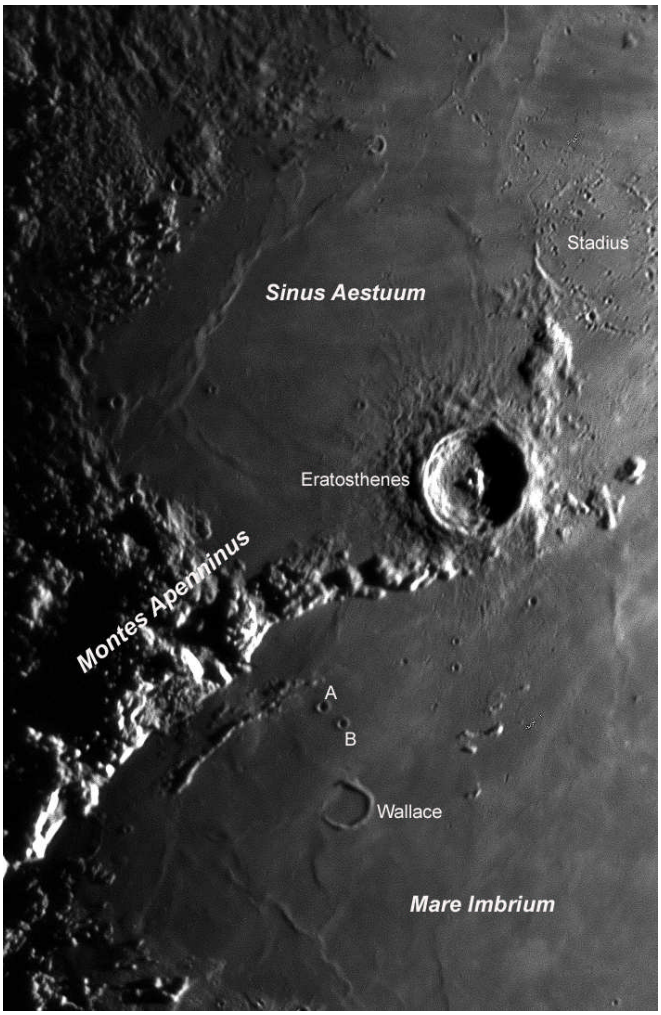

Guide map to Plate 1

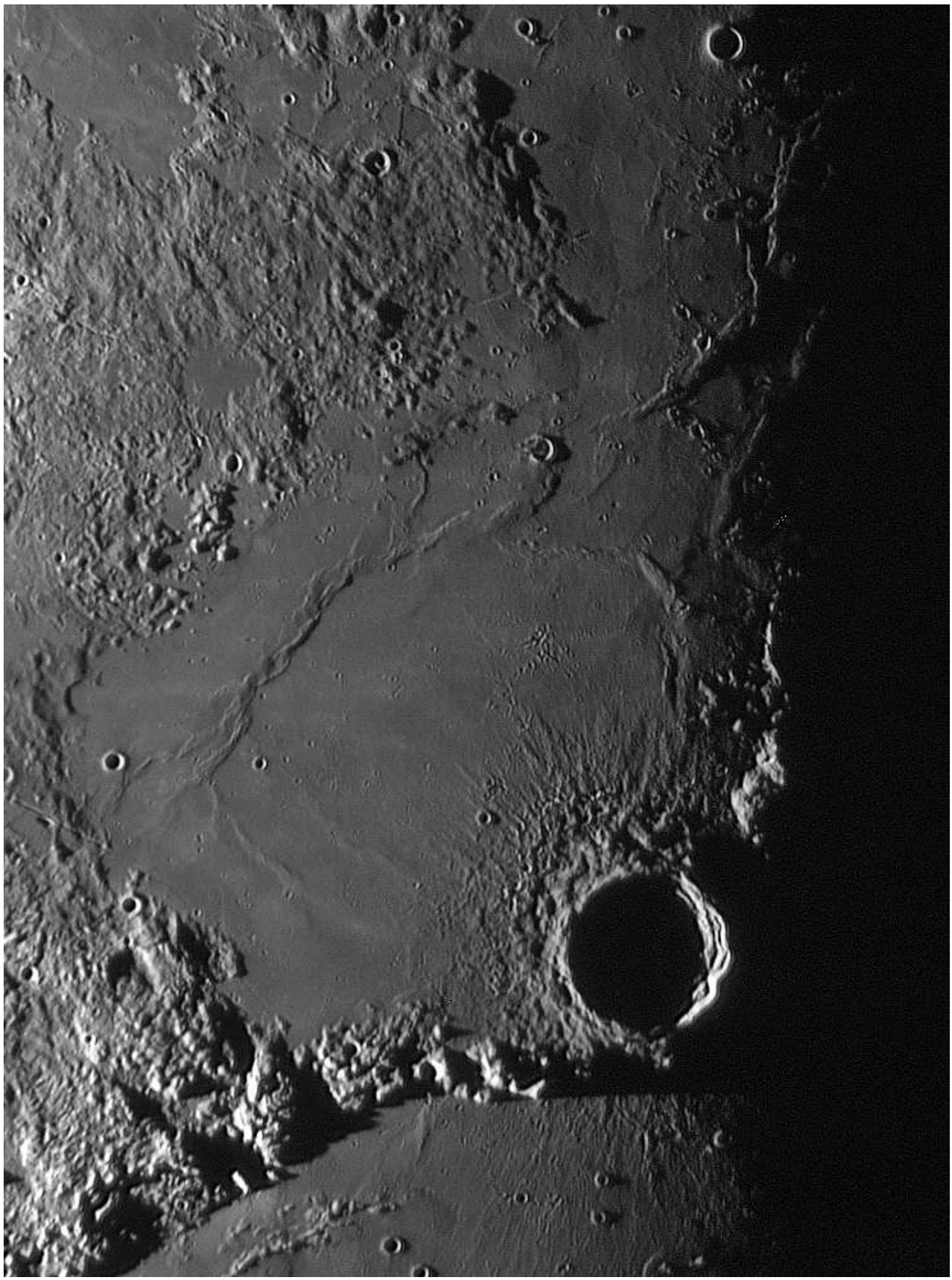

Plate 1-1 20090203 12h14m Colongitude: 13

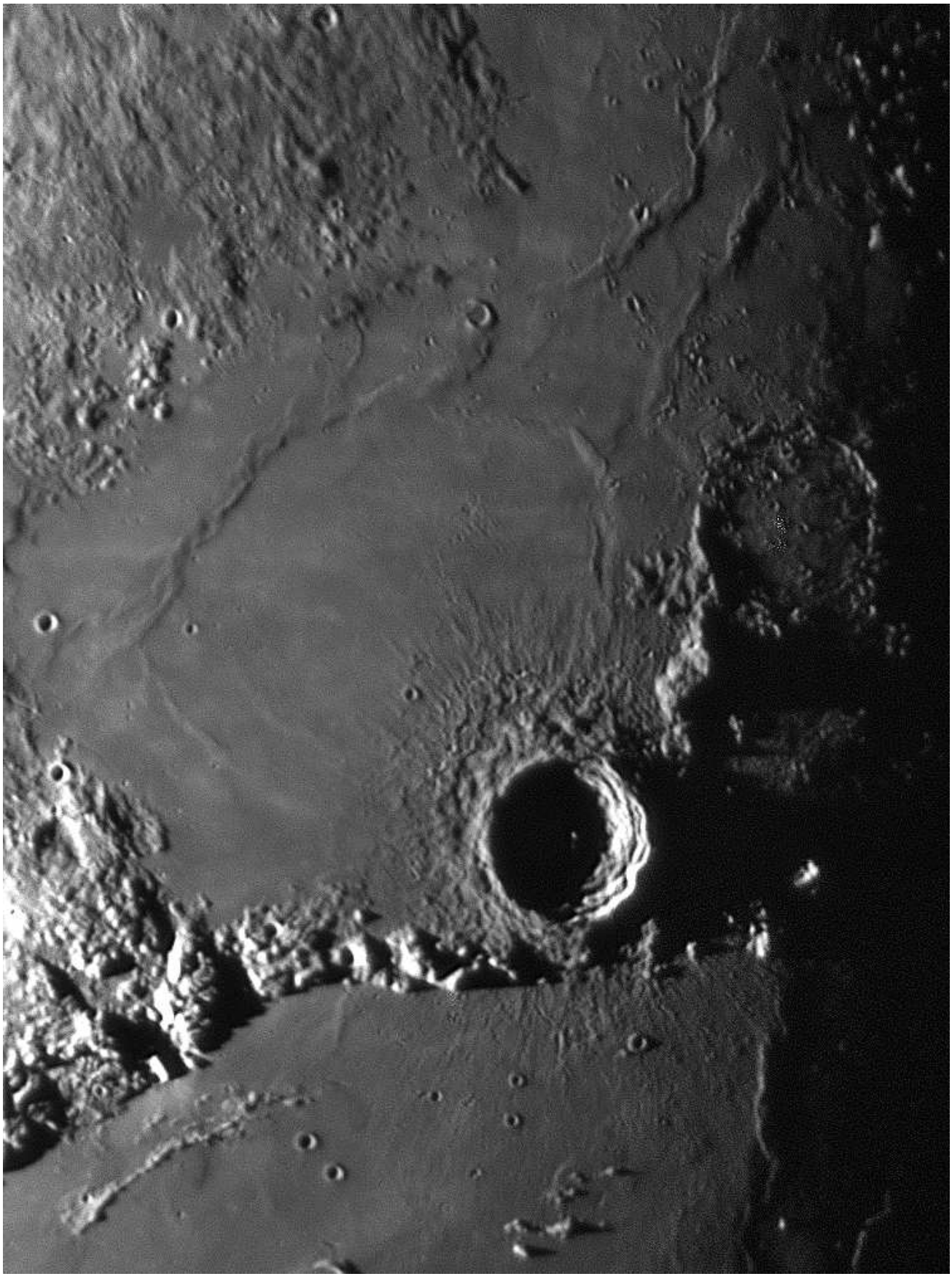

Plate 1-2 20110511 13h38m Colongitude: 15

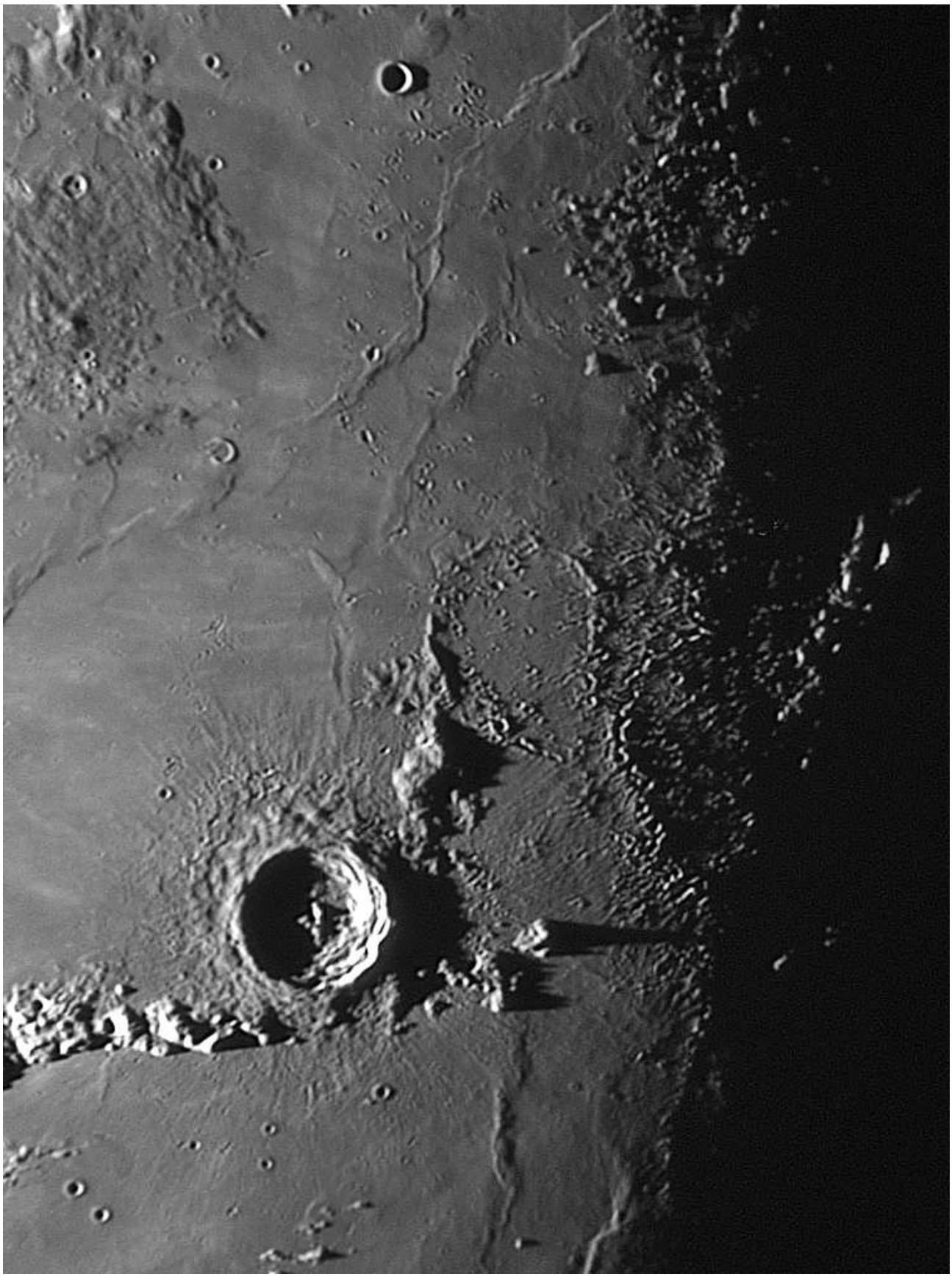

Plate 1-3 **20110113** **11h46m** **Colongitude: 16**

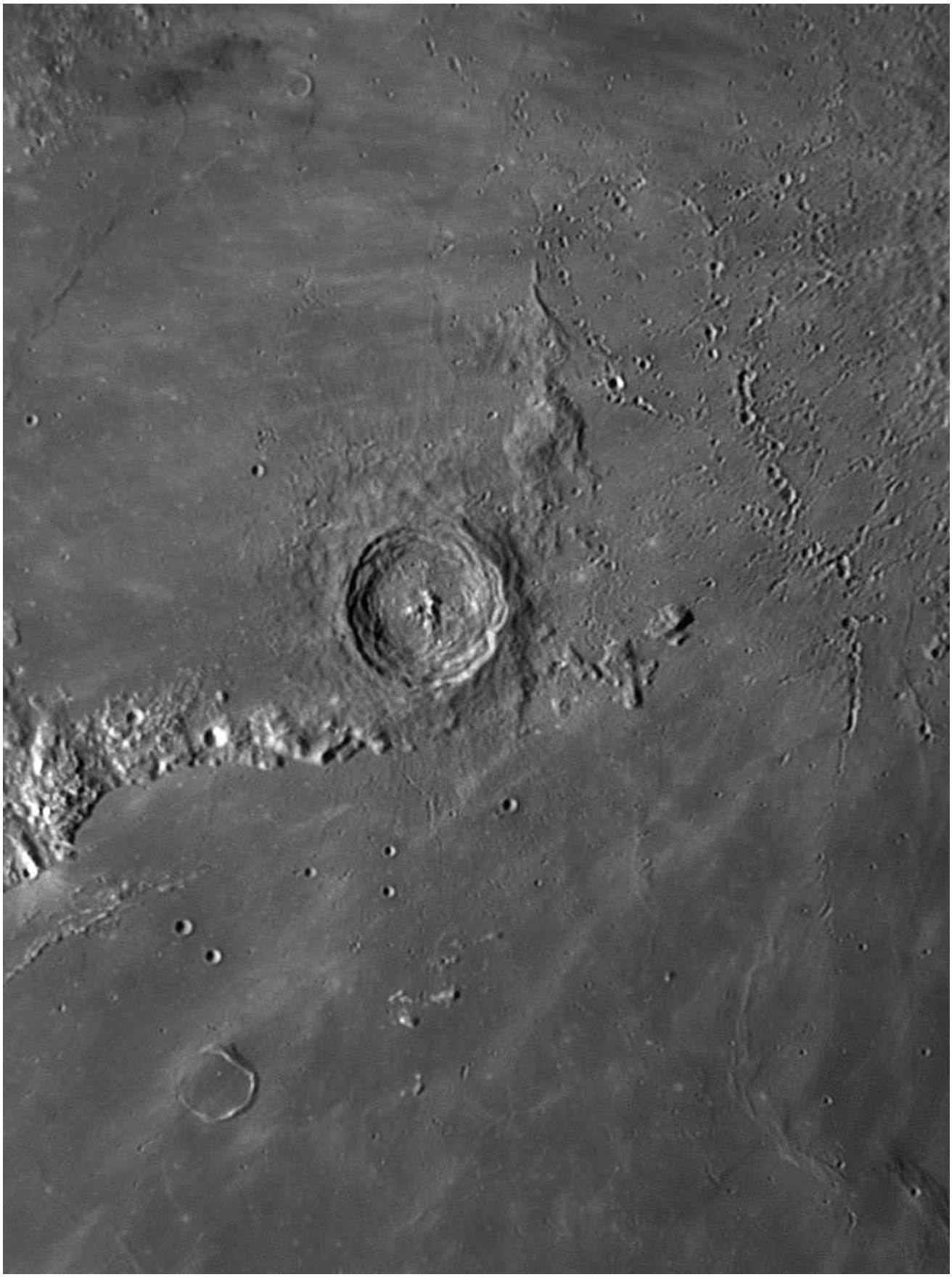

Plate 1-4 **20110413** **12h28m** **Colongitude: 33**

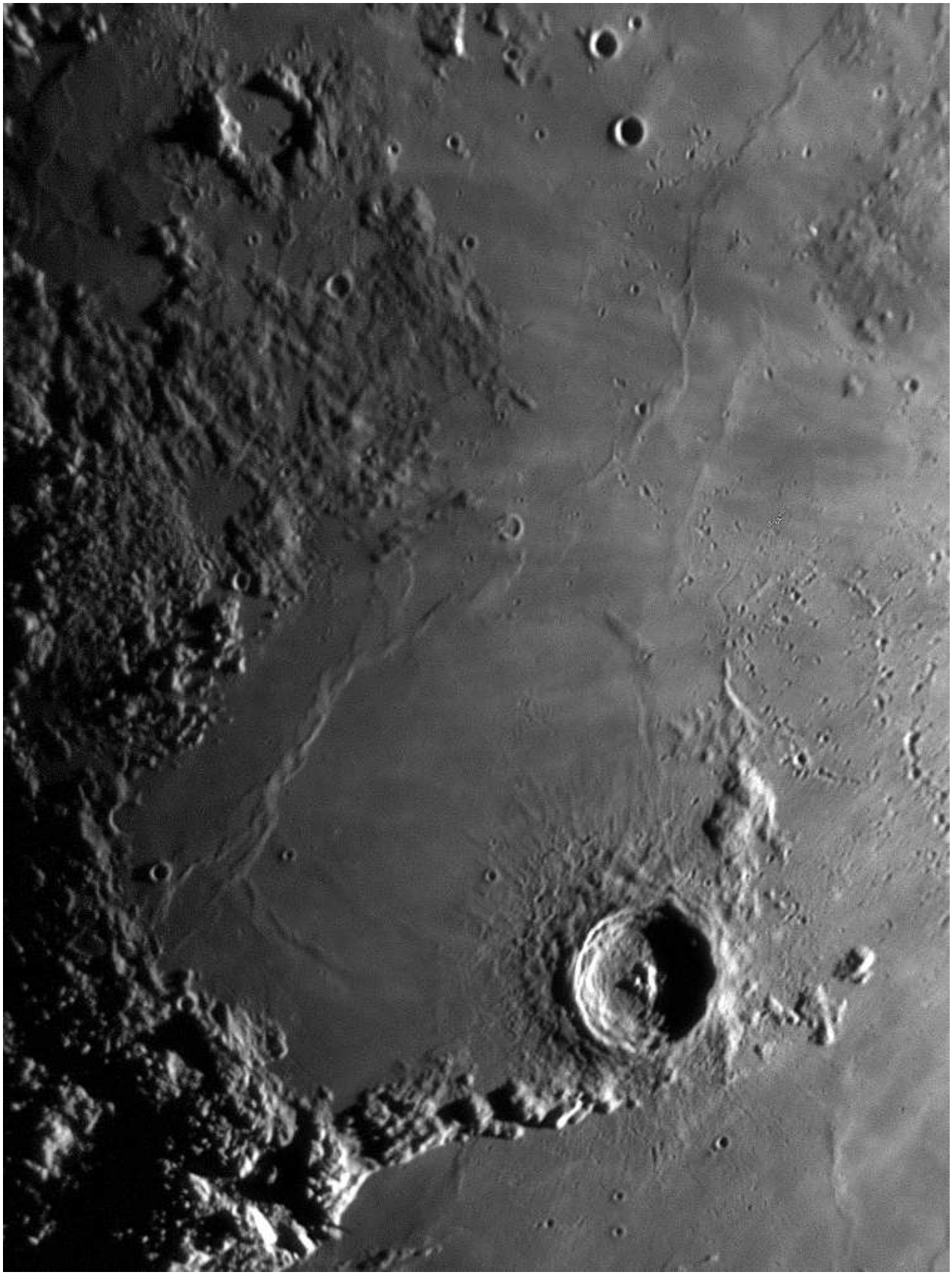

Plate 1-5 20110425 21h28m Colongitude: 183

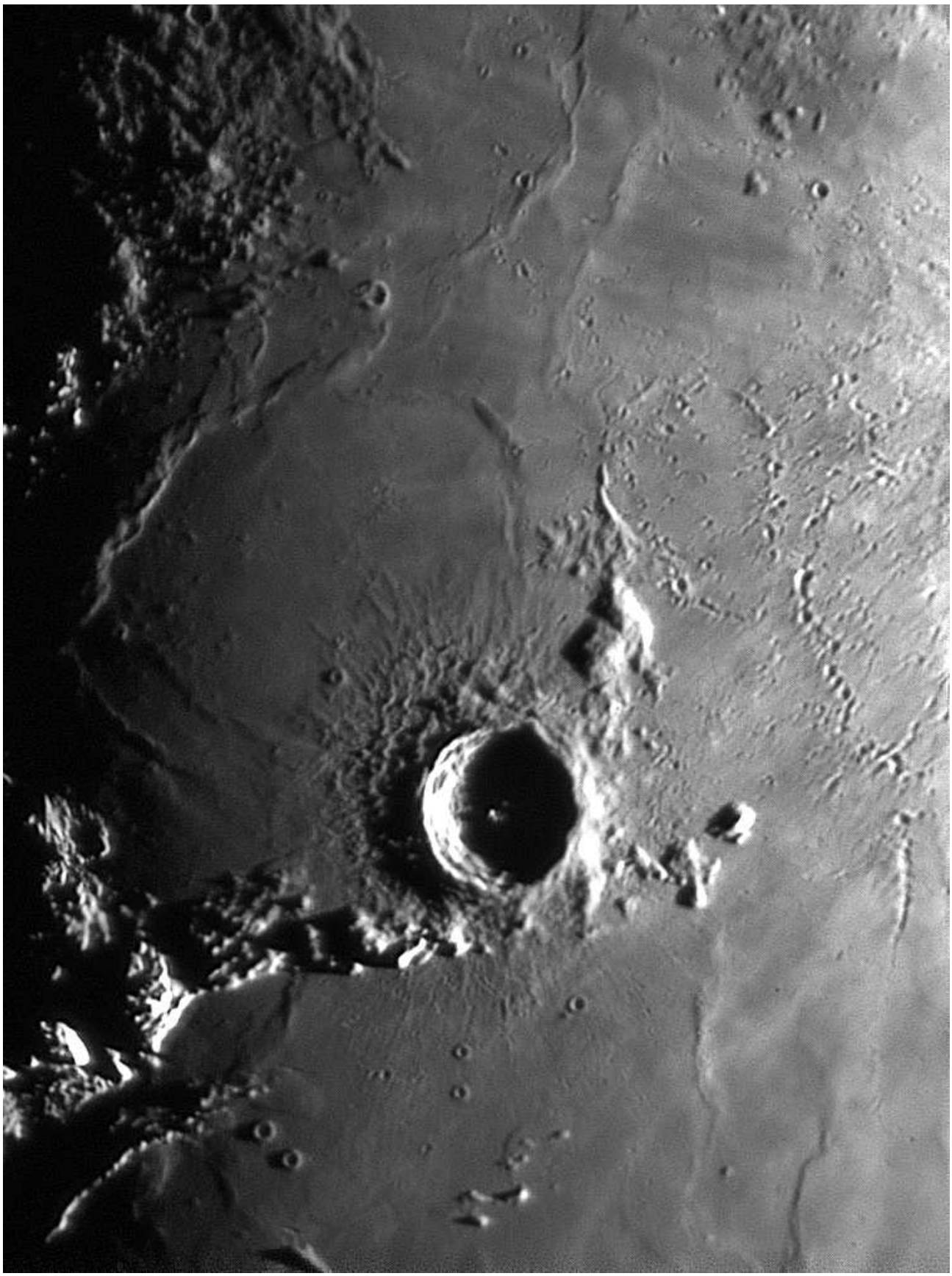

Plate 1-6 **20101228** **21h39m** **Colongitude: 186**

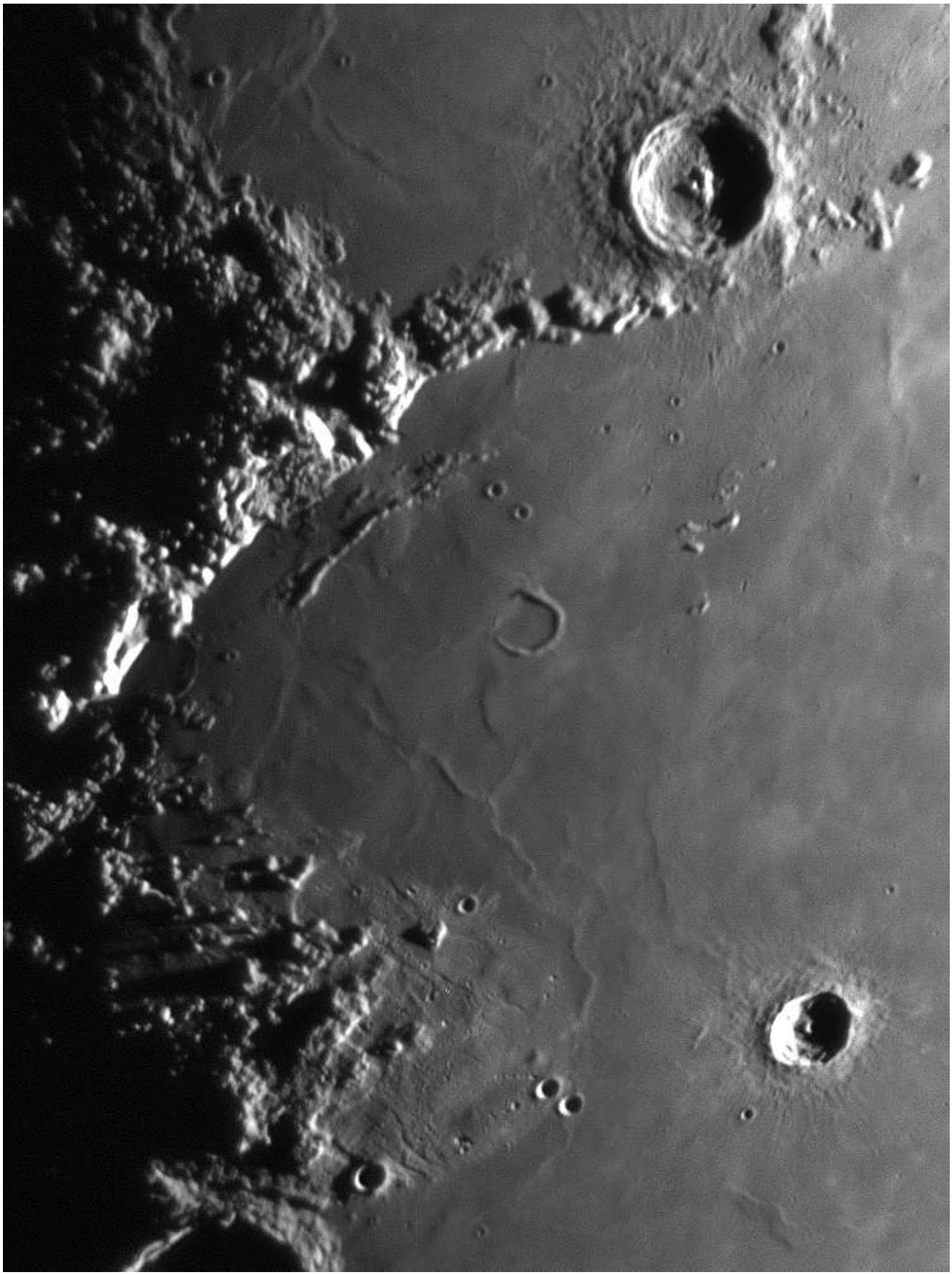

Plate 1-7 20110425 21h26m Colongitude: 183

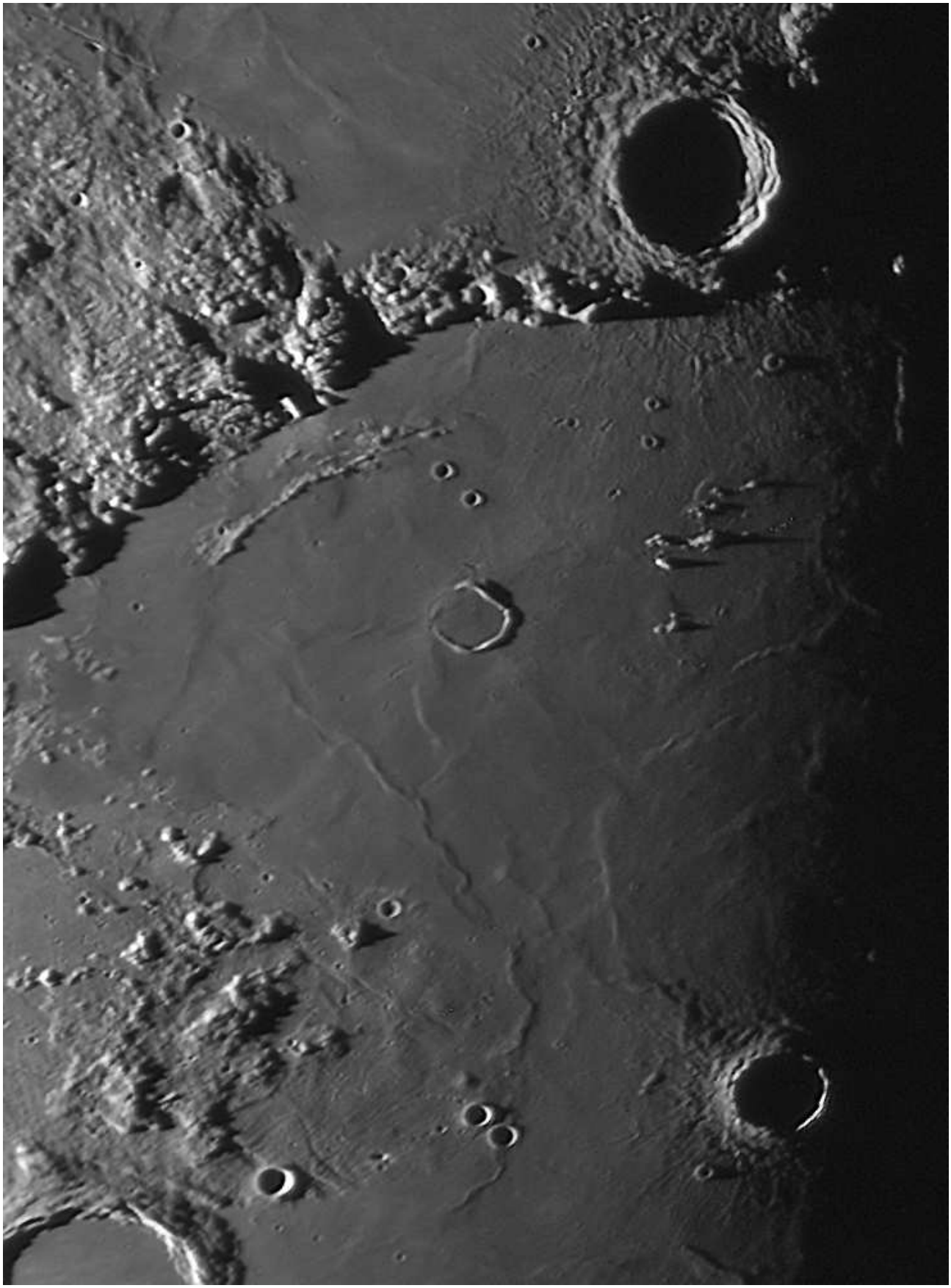

Plate 1-8 **20090203** **13h57m** **Colongitude: 13**

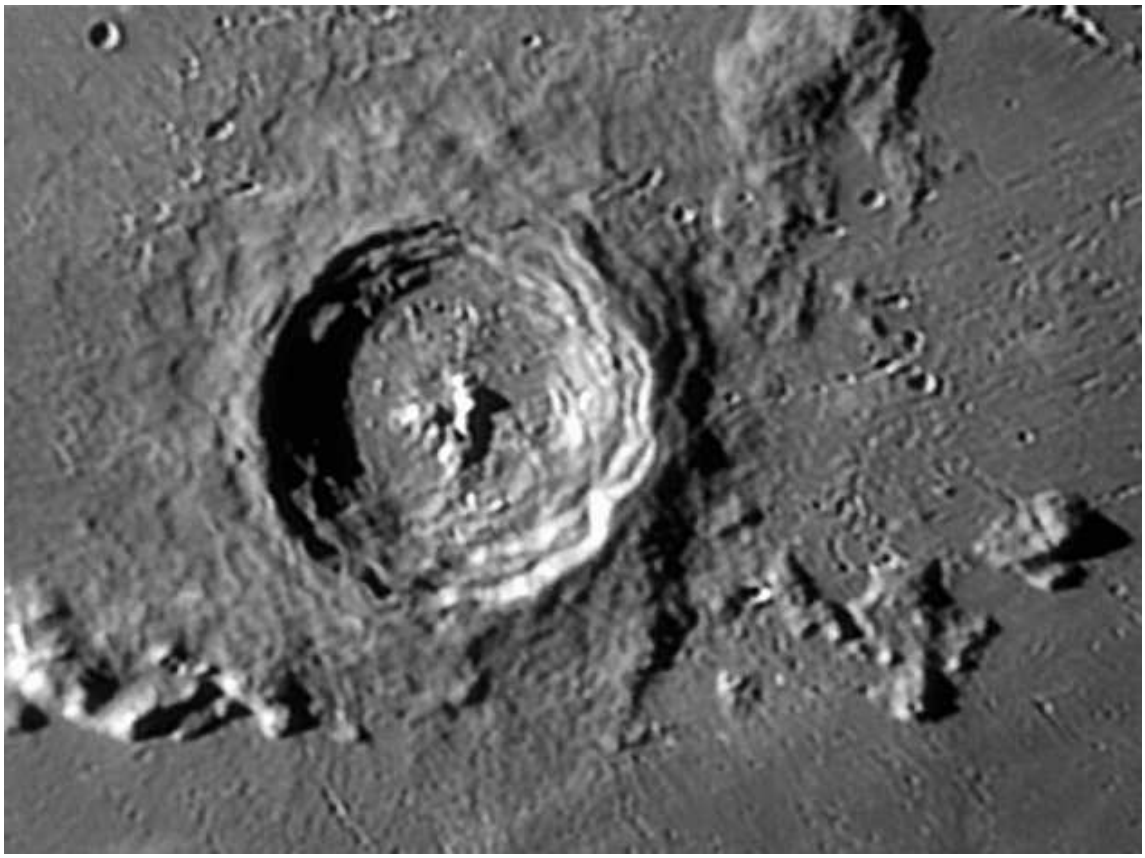

Fig. 1 Eratosthenes 20050418 12h44m Colongitude: 23

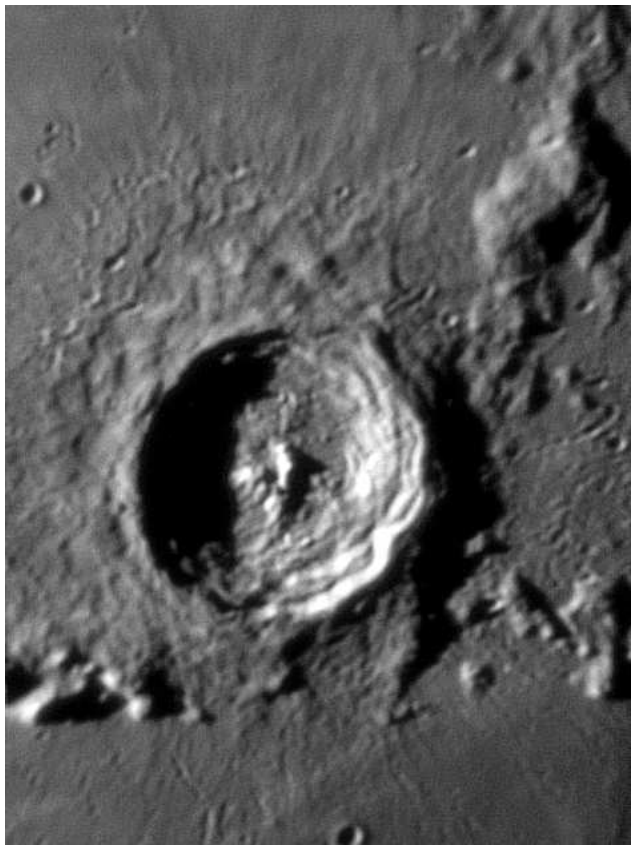

Colongitude: 11 Colongitude: 19

Fig. 2 The east glacis of Eratosthenes looks rougher under early sunlight

Under Morning and Evening Illumination

Colongitude: 23

Colongitude: 179

Fig. 3 Stadius

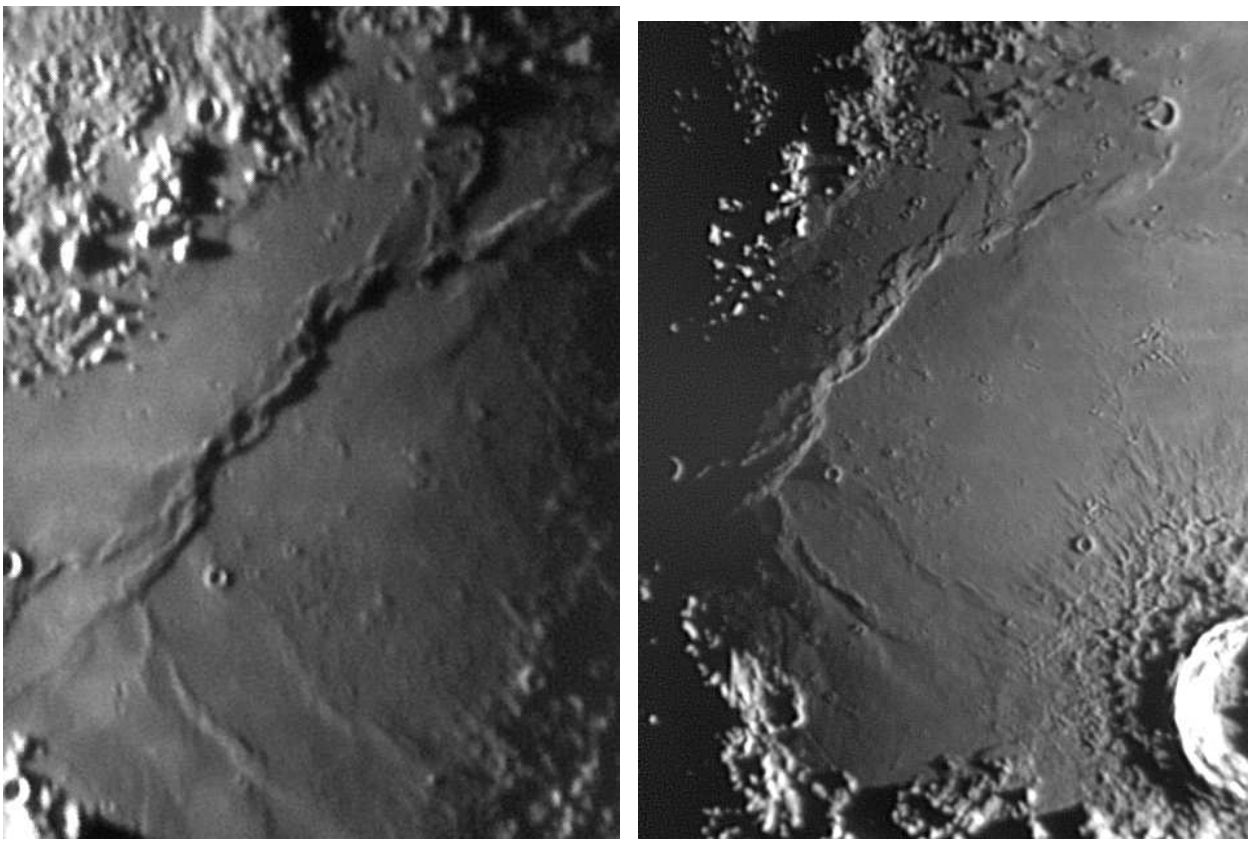

Colongitude: 9 Colongitude: 185

Fig. 4 Closer look of braided ridges in east of Sinus Aestuum

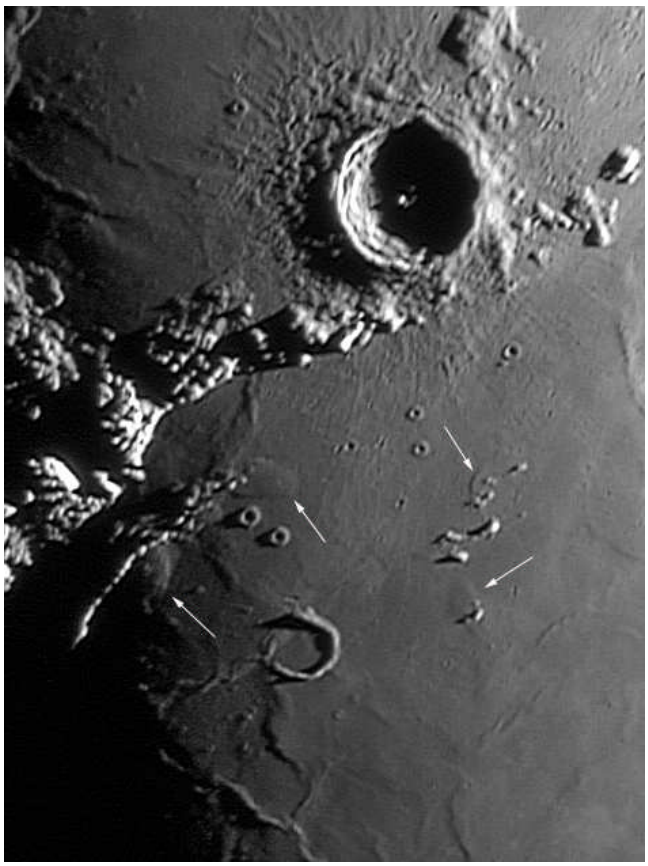

20040213 21h13m Colongitude:186

20031216 22h37m Colongitude: 189

Fig. 5 Domes found in Eratosthenes region

Lunar Mosaic

Maginus to Deslandres

20090203 11h49~50m

Colongitude: 12

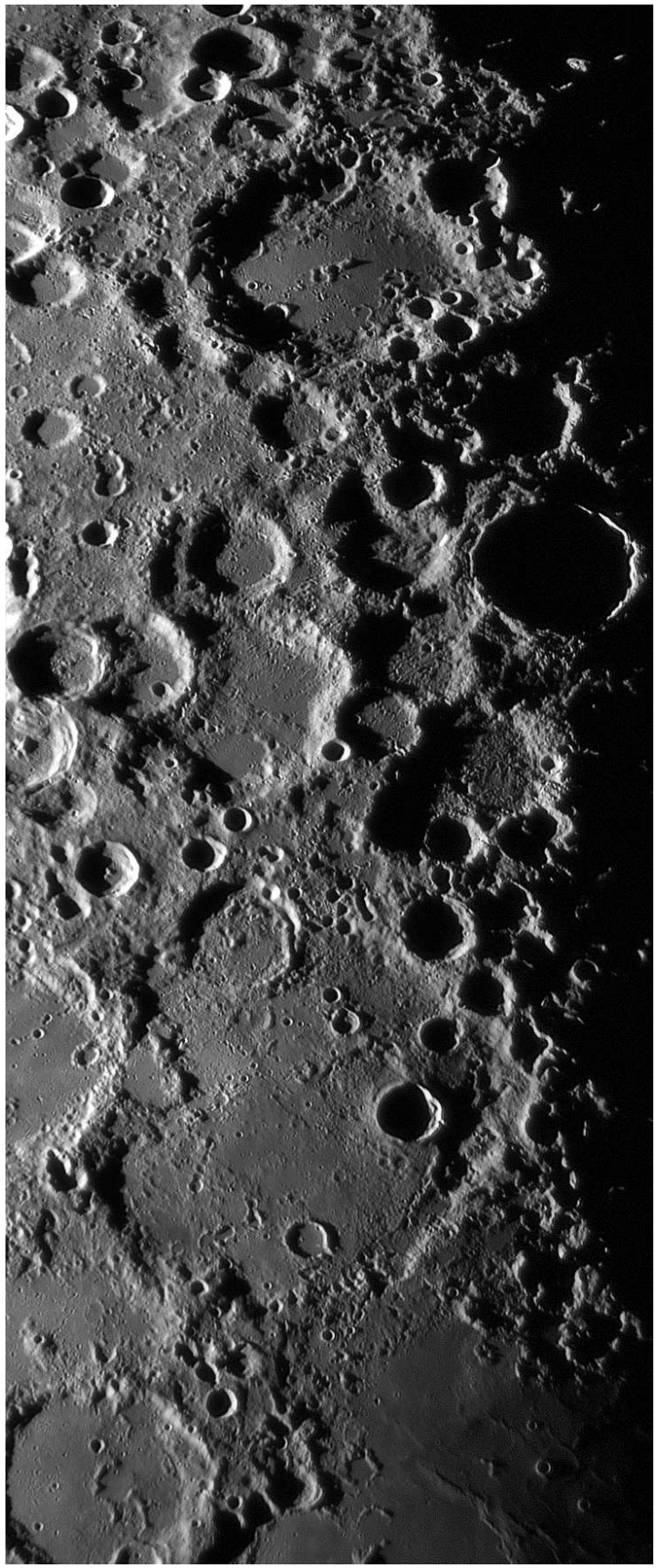

Back cover of the album

Photographic Lunar Album

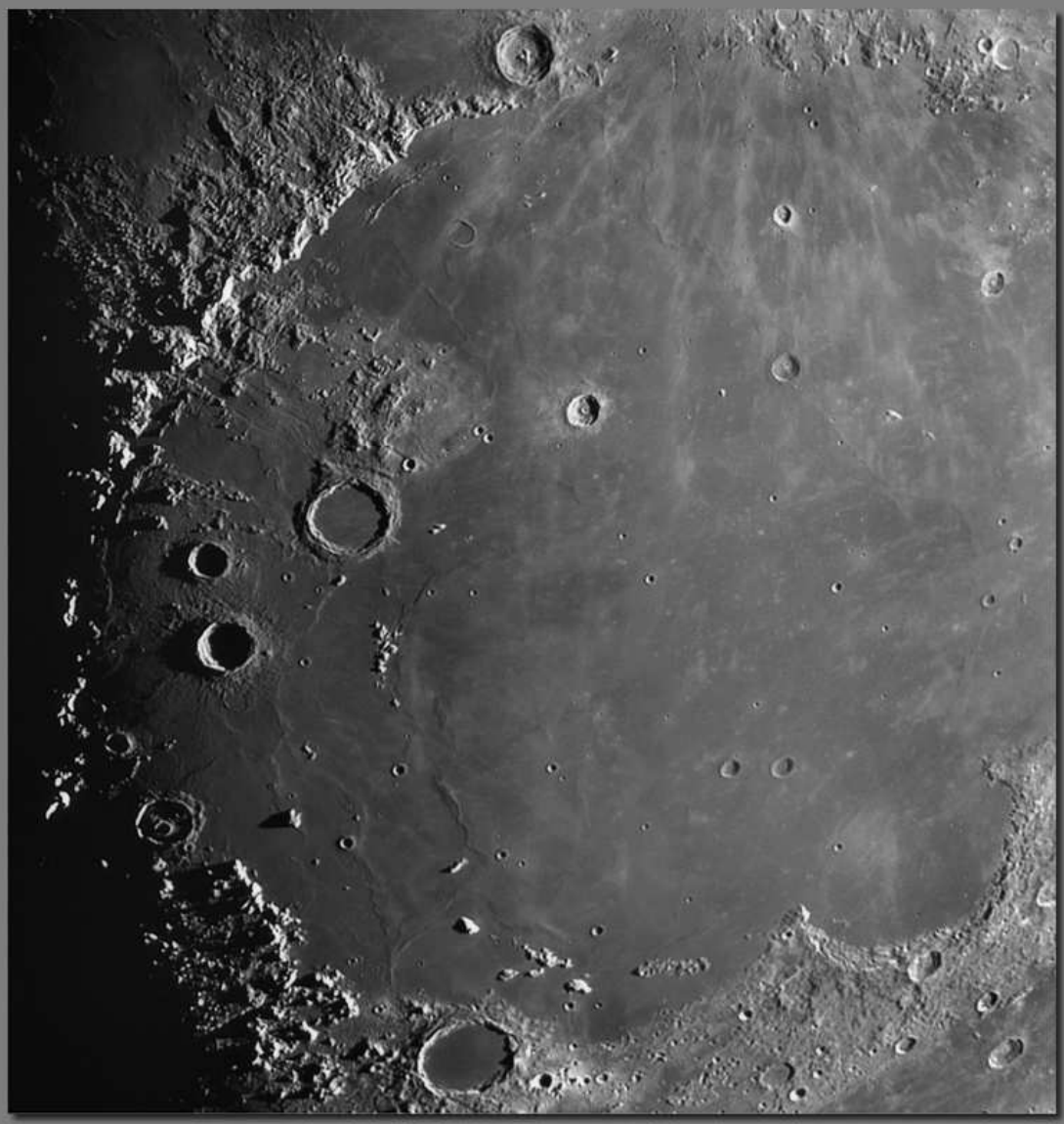

Study of a shallow dome near the lunar crater Autolycus

by Raffaello Lena, Jim Phillips and Paolo Lazzarotti

Geologic Lunar Research (GLR) group

Abstract

In this article we describe the morphometric and rheologic results for a shallow and large dome on the Moon situated to the east of Autolycus crater. The selenographic coordinates are determined to 30.50° N and 3.82° E. This flat dome, which we termed Autolycus 1 (Aut1), has a base diameter determined as 28.0 km. Using an image-based photoclinometry approach to reconstruct the three-dimensional shape of Aut1, we find that its height amounts to 75 ± 10 m, resulting in an average flank slope of 0.31°. The edifice volume is determined to 23 km³. According to the morphometric properties, the dome belongs to class C_1 in the classification scheme for lunar domes introduced in previous studies.

1. Introduction

The apparent internal origin of lunar domes was a major factor in endogenic interpretations of the maria, and their low profiles suggest a volcanism characteristic of fluid mafic magmas (Wilhelms, 1987). The Geologic Lunar Research (GLR) group has an ongoing project to study lunar domes with the purpose of their classification based on rheologic properties. The Consolidated Lunar Dome Catalogue published online (Lena and Wöhler, 2008) contains all lunar domes which have been studied in detail by the GLR group and for which reasonably accurate morphometric properties could be determined. The catalogue is continuously updated according to ongoing observing and modelling activities.

In previous works we have introduced a novel classification scheme for effusive lunar domes which is based on their spectral and morphometric properties, and have examined for a variety of lunar mare domes the relationship between the conditions in the magma source regions and the resulting eruption conditions at the surface (Wöhler et al., 2006; Wöhler et al., 2007; Wöhler and Lena, 2009, Lena et al., 2011). The typical hemispherical or flat mound with summit pit is widely accepted to be the lunar equivalent of terrestrial small shield volcanoes (Head and Gifford, 1980) Many other lower rises have more gentle slopes and lack the summit pit and sometimes the roughly

circular outlines of classical domes.

In this paper, our goal is to assess the evidence for a shallow lunar dome termed Autolycus 1 (Aut1). We examine the morphometric characteristics by making use of a combined photoclinometry and shape from shading approach (cf. Lena et al., 2006; Wöhler et al., 2006).

Due to its low profile, Lunar Orbiter and Clementine images do not show it very well, due to the typically high solar angle under which these images were acquired. Hence, as part of our program of observing and cataloguing lunar domes, we have used high-resolution telescopic CCD images taken under oblique illumination conditions.

2. Ground-based observations

2.1 Visual observations

On the evening of May 12, 1989, using a 6" F/12 apochromatic refractor to search the terminator, Phillips came across a low dome-like structure immediately East of Autolycus (cf. Fig. 1a). Notes from his logbook read: **May 12, 1989** 9:20- EDT Seeing Conditions: 6-7/10. "The weather appears unwilling to cooperate with observations of the Moon lately. Viewing between clouds with some large breaks. Noted a dome-like swelling E of Autolycus just into the Mare Imbrium. Marked the area on the Times Atlas. Fair turbulence but I am able to get a few nice glimpses. Hyginus Rille and Triesnecker near terminator. Able to use 12mm and 16mm Naglers with and without Barlow (114X, 152X, 205X and 274X) in spite of the seeing and the clouds. Spent a fair amount of time observing the dome-like structure near Autolycus. The more I observe it, the more convinced I am that it is a true dome. Worked hard to get the position drawn as accurately as possible on The Times Atlas. Cool evening. Needed a lined wind-breaker. Mosquitoes were around but they were too sluggish to be of any concern".

Observing the Moon on May 29, 2001 with a 9" F/15 apochromatic refractor Phillips noted two domes, one near Manilius and the previously observed dome E of Autolycus (cr. Fig. 1b).

May 29, 2001 8:30 – 10:00 PM EDT. Seeing Conditions: 7/10. "Out early to observe the Moon. Terminator is just W of Triesnecker. Rille system is prominent. F & G easily seen. Third craterlet South of F and West of G noted. In spite of the turbulence 32mm Plossls plus the binoviewer provide a very nice view. Up to Manilius. West of manilius

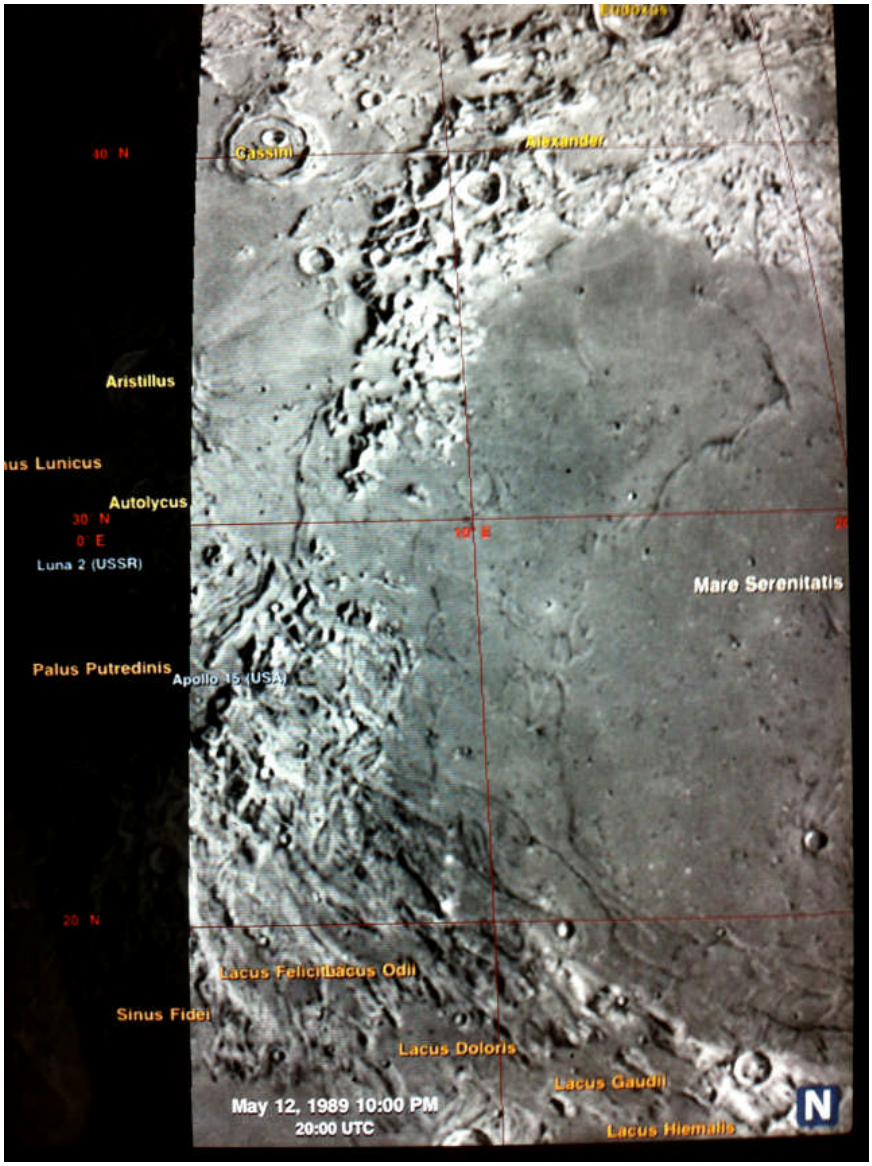

Figure 1a. Observation by J. Phillips (see text for detail).

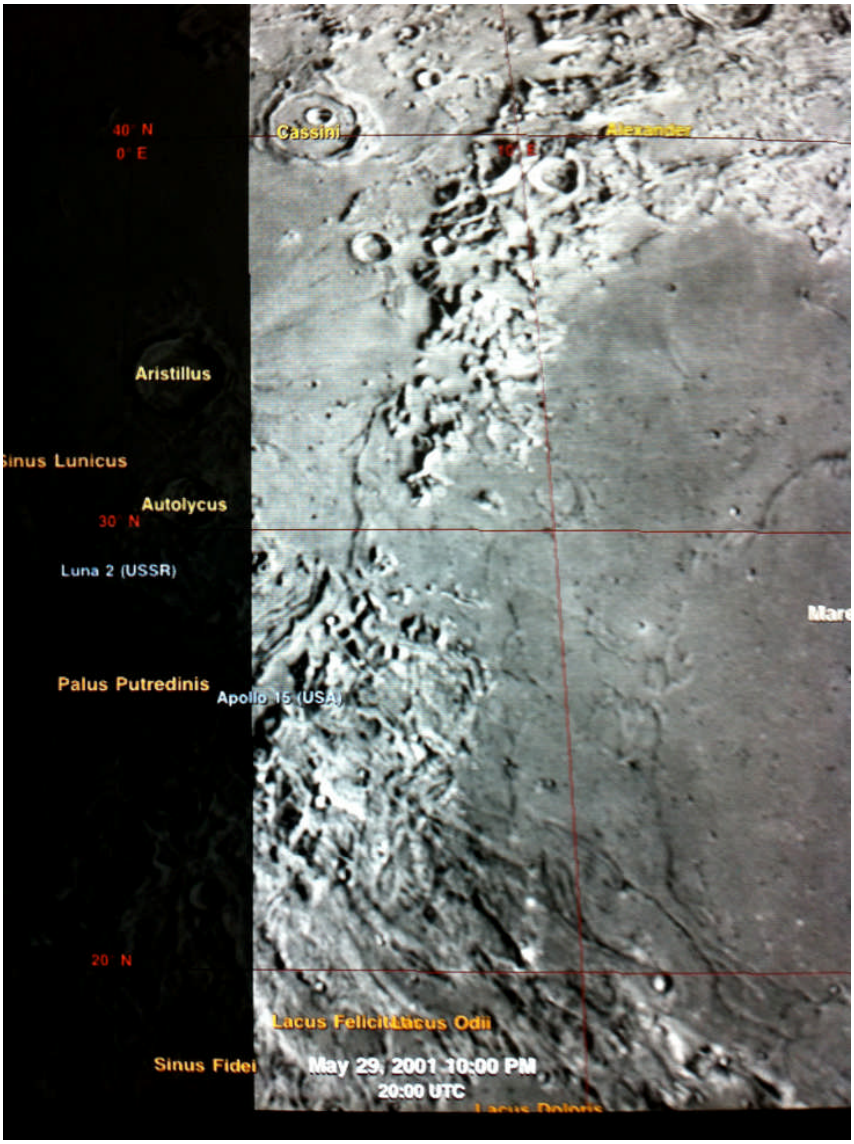

Figure 1b. Observation by J. Phillips (see text for detail).

Figure 1c. Observations by J. Phillips (see text for detail).

in the Mare Vaporum is a dome. I marked it in my Times Atlas of the Moon. I had previously marked it February 24 (?) 1988 with my 8" achromatic refractor. The "Hill" NW of Hyginus was observed. Although I might have missed it if I had not noted it on the Times Atlas first I could actually glimpse the tiny craterlet on the summit! E of Aristillus and Autolycus Rima Theaetetus noted. Next to Caucasus Montes, on a lava flow or mound Luna 2 landing site in shadow. Rima Fresnel noted. Hadly Rille in shadow. Dome East of Autolycus noted. First seen with 6" F/12 5/12/89" (cf. Fig. 1c).

2.2 CCD images

Telescopic CCD images of the dome Aut1, examined in this study, are shown in Fig. 2a-d. The images were taken under oblique illumination conditions and are oriented with north to the top and west to the left. Data about date, time (UT) and instruments are reported in Table 1. Using the Lunar Terminator Visualization Tool (LTVT) software package (Mosher and Bondo, 2006) we determined the selenographic positions of the examined dome to 30.50° N and 3.82° E. LTVT is a freeware program that displays a wide range of lunar imagery and permits a variety of highly accurate measurements in these images. Selenographic coordinates, sizes, and shadow lengths of features can be estimated based on a calibration procedure. This calibration allows LTVT to make the spatial adjustments necessary to bring the observed positions of lunar features into conformity with those expected from the Unified Lunar Control Network (ULCN). The ULCN is a set of points on the lunar surface whose three-dimensional selenodetic coordinates (latitude, longitude, and radial distance from the lunar centre) have been determined by careful measurement. Typically these points consist of very small craters. According to Davies et al. (1994), the three-dimensional positions are expressed in the mean Earth/polar axis system.

3. Clementine imagery: Surface composition

For spectral analysis we utilise the Clementine UVVIS five-band data set as published by Eliason et al. (1996). For all spectral data extracted in this study, the size of the sample area on the lunar surface was set to 3×3 km^2. Variations in soil composition, maturity, particle size, and viewing geometry are indicated by the reflectance R_{750} at 750 nm wavelength. Another important spectral parameter is the R_{415}/R_{750} ratio, which is correlated with the variations in TiO_2 content of mare soils. A corresponding relation was

established by Charette et al. (1974), specifically regarding different basaltic units in Mare Tranquillitatis. A comprehensive characterisation of spectral features attributable to titanium in lunar soils is provided by Burns et al. (1976). Relying on TiO_2 abundance data obtained with the Lunar Prospector neutron spectrometer, Gillis-Davis et al. (2006) demonstrate that other factors such as ilmenite grain size or FeO content may give a significant contribution to the UV/VIS ratio. According to these analyses, TiO_2 content is monotonously increasing with R_{415}/R_{750} ratio, but the correlation is only moderate and the data display a strong scatter. The third regarded spectral parameter, the R_{950}/R_{750} ratio, is related to the strength of the mafic absorption band, representing a measure for the FeO content of the soil and being also sensitive to the optical maturity of mare and highland materials (Lucey et al., 1998). Clementine UVVIS imagery indicates a 750 nm reflectance of R_{750} = 0.1479, a moderate value for the UV/VIS colour ratio of R_{415}/R_{750} = 0.6012, indicating a moderate TiO_2 content, and a high R_{950}/R_{750} ratio of 1.0319 indicating a high optical maturity and thus a high exposure age of the dome surface. The absence of a spectral contrast between Aut1 and the surrounding surface indicates that the dome is not a piece of pre-existing elevated terrain later embayed by basaltic lava, a so-called kipuka.

4. Lunar Orbiter and WAC (LRO) imagery

As very low solar illumination angles are required to reveal the gentle slopes of lunar domes, most of these subtle structures do not appear in the available sets of orbital images, e.g . Lunar Orbiter imagery and the Lunar Reconnaissance Orbiter (LRO) WAC (cf. Fig. 3).

5. Morphologic and morphometric properties

5.1 Shadow length measurements

From the shadow length l, corrected for foreshortening, and the local solar altitude μ the height h of a dome is given by (1)

$$h = l \tan \mu \qquad (1)$$

The average slope ξ is then calculated by (2)

$$\xi = \mathrm{INV} \tan (h / R) \qquad (2)$$

where R is the radius of the dome and h its height.

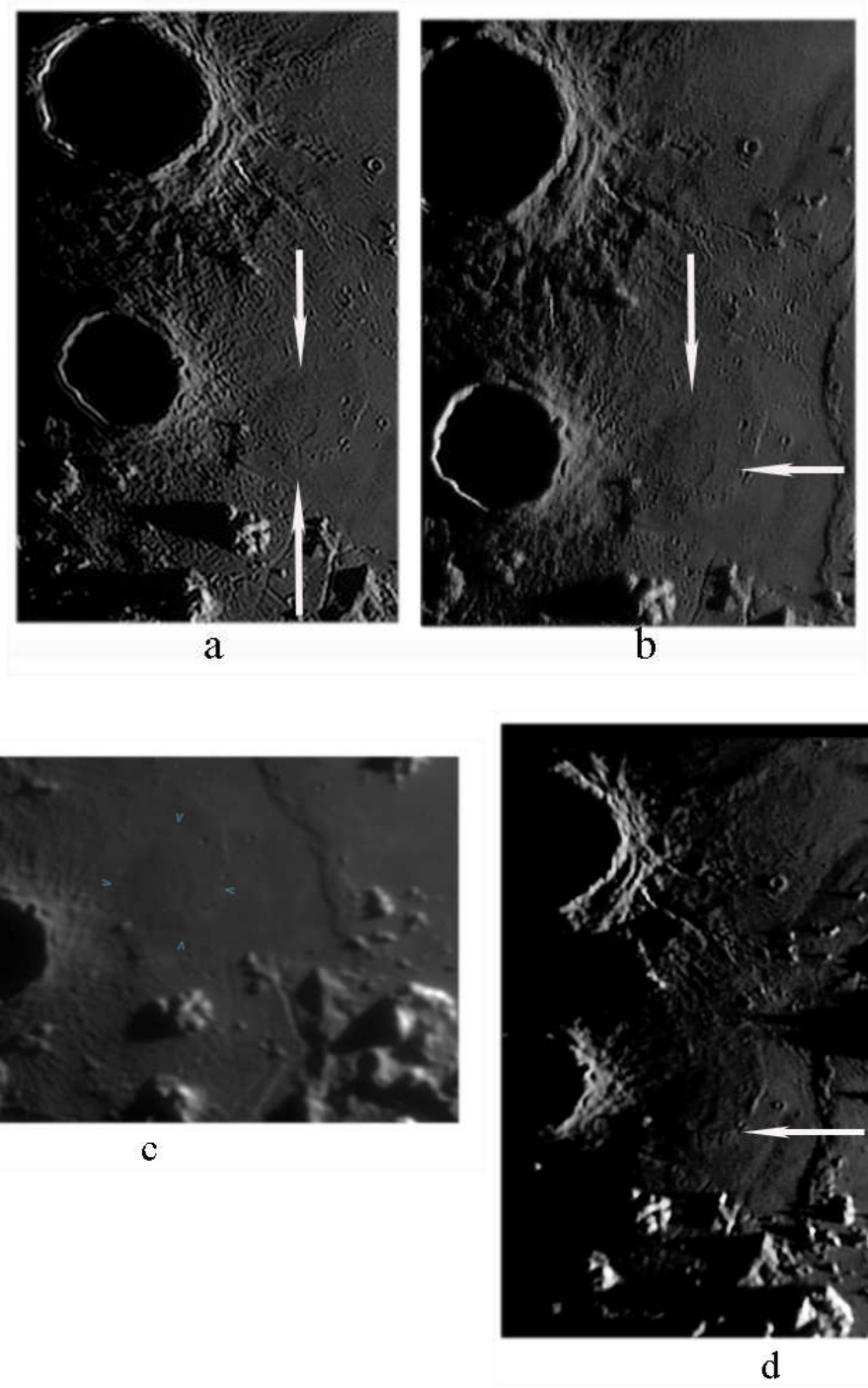

Figure 2: Telescopic CCD images of the lunar dome Autolycus 1. (a) April, 10, 2011 20:03 UT. (b) April, 24, 2007 19:22 UT. (c) May, 21, 2010 02:28 UT. (d) May, 1, 2009 19:30 UT.

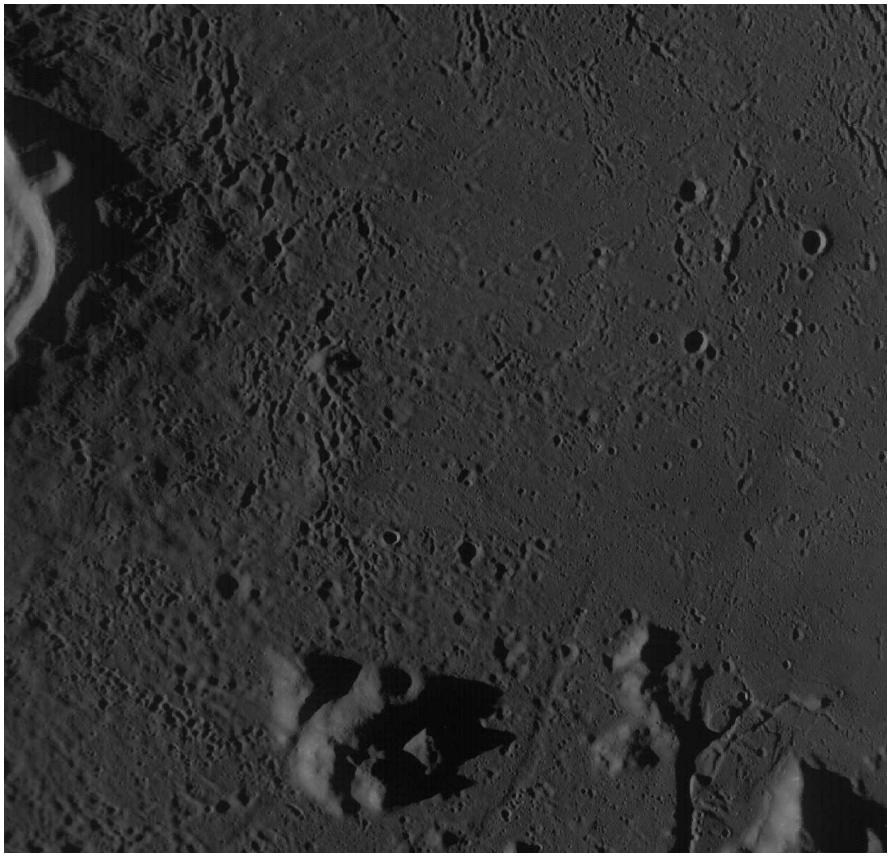

Figure 3: WAC image M117467790ME of the examined region.

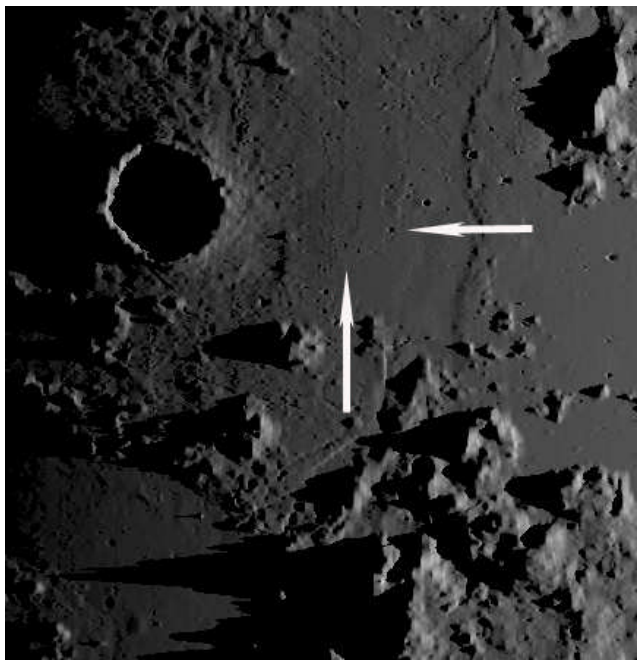

Figure 4. Image simulated based on the LOLA DEM using LTVT, assuming the same illumination conditions as in Fig. 1a.

In this study, we initially computed the shadow length to determine the height of the examined dome using the image of Fig. 2d, where Aut1 is imaged under strongly oblique illumination, and the Lunar Terminator Visualization Tool (LTVT). For the dome Aut1, closed to the terminator, a height of 70 ± 10 m was obtained. This result, based on shadow length measurement, yields slope and height value consistent with those obtained by the image-based 3D reconstruction approach described in Sections 5.2.

5.2 Digital elevation map

Generating an elevation map of a part of the lunar surface requires its three-dimensional (3D) reconstruction. Recently, a global lunar digital elevation map (DEM) obtained with the Lunar Orbiter Laser Altimeter (LOLA) instrument on the Lunar Reconnaissance Orbiter (LRO) spacecraft has been released.

It has a lateral resolution of 1/64 degrees or about 500 m in the equatorial regions of the Moon (http://pds-geosciences.wustl.edu/missions/lro/lola.htm).

A section of the LOLA DEM displaying the region around the dome Autolycus 1 is shown in Fig. 4, a rendered image obtained using LTVT and assuming the same illumination conditions as in Fig. 2a. In the LOLA DEM, the elevation difference between the dome centre and its western border, corresponding to about 70 m, may be regarded as an approximate value of the dome height.

We have also generated an elevation map of the dome based on our telescopic CCD image. A well-known image-based method for 3D surface reconstruction is shape from shading (SfS). The SfS approach aims for deriving the orientation of the surface at each image location by using a model of the reflectance properties of the surface and knowledge about the illumination conditions, finally leading to an elevation value for each image pixel (Horn, 1989).

The dome Autolycus 1 has a circular diameter of 28 km and a corresponding circularity (minor axis divided by major axis) of 0.99. The dome shows an elongated depression on its summit, not well defined in the probe images (Fig. 3).

Its height was determined to 75 ± 10 m using the image shown in Fig. 1b, resulting in an average flank slope of 0.31° ± 0.03°. A cross-sectional profile of the dome is shown in Fig. 5. Assuming a parabolic dome shape the edifice volume corresponds to 23 km³. The morphometric properties inferred for the dome Aut1 are summarised in Table 2.

Figure	Telescope/Camera	Date Time UT	Observer
2a	Mak-Cassegrain 178 mm Lumenera LU 075M	April, 10, 2011 20:03 UT	Lena R
2b	Gladius XLI 400mm Cas-segrain Experimental ICX285	April, 24, 2007 19:22 UT	Lazzarotti P.
2c	TEC 200 mm Atik CCD camera	May, 21, 2010 02:28 UT	Phillips J.
2d	Mak-Cassegrain 178 mm Lumenera LU 075M	May, 1, 2009 19:30 UT	Lena R.

Table 1

Dome	long. [°]	lat. [°]	slope [°]	D [km]	h [m]	V [km³]	class
Aut1	-23.82°	-28.30°	0.31	28	75	23	C_1

Table 2: Morphometric properties of the dome Aut1 described in this study.

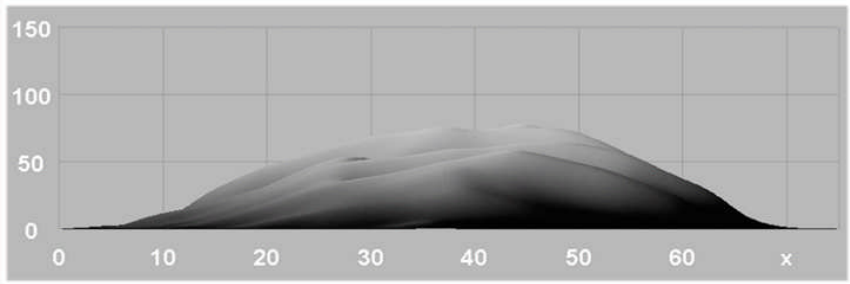

(a)

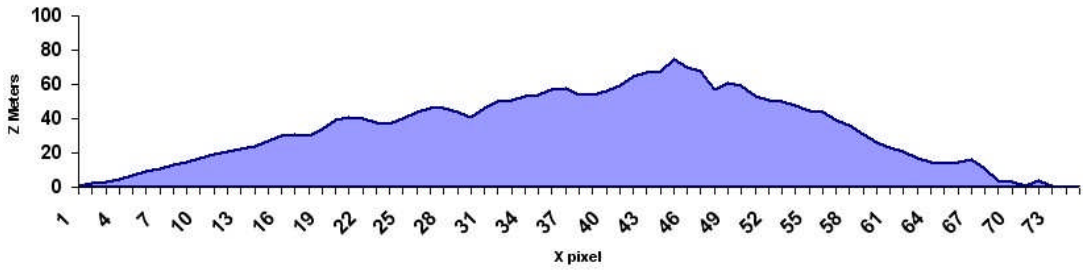

(b)

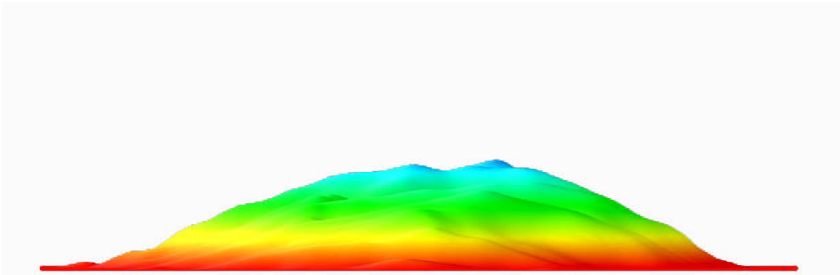

(c)

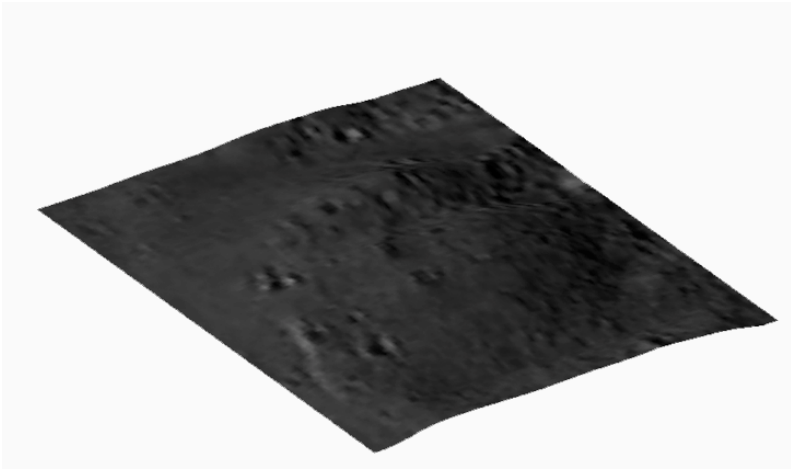

(d)

Figure 5. (a-c) Cross-sectional profile of Autolycus 1. The vertical axis in the three profiles is 30 times exaggerated, the curvature of the lunar surface has been subtracted. (d) Refined DEM of the dome Aut1 obtained based on the image of Fig. 1b superimposed onto the corresponding DEM.

6. Modelling of feeder dike dimensions

Knowledge about the morphometric properties of lunar domes (diameter, height, volume) allows to estimate the rheologic properties of the magma which formed the effusive domes, i.e. its viscosity η and eruption rate E as well as the duration of the effusion process T*e* (Wilson & Head, 2003). Mare volcanic eruptions were fed from source regions at the base of the crust or deeper in the lunar mantle. In this scenario, pressurised magma produces narrow elongated fractures in the crust, the so-called dikes, through which it ascends towards the surface. The rheologic parameters of lunar effusive domes allow to estimate the magma rise speed U as well as the width W and length L of the feeder dike of a dome (Wilson & Head, 2003), where as a general rule the vertical extension of a dike into the crust approximately corresponds to its length (Jackson et al., 1997). The model has been described in detail by Wilson & Head (2003).

7. Results and discussion

Four classes termed A, B, C, and E describing monogenetic mare domes are established essentially according to the diameter, flank slope, volume of the dome edifice and the TiO_2 content of its soil (cf. Wöhler et al, 2006; Wöhler et al, 2007). In this classification scheme, domes of class C have diameters between 8 and 20 km, with relatively low flank slopes typically below 2°. Domes formed from spectrally red lavas of low to moderate R_{415}/R_{750} ratio with large diameters between 13 and 20 km and large edifice volumes of several tens of km^3 are assigned to subclass C_1, while domes with smaller diameters between 8 and 13 km and lower edifice volumes are assigned to subclass C_2. The morphometric properties represented by candidate intrusive domes, described as classes In1-In3 by Wöhler & Lena (2009), can overlap with the values characterising several classes of effusive domes. A reliable discriminative criterion, however, is the circularity c of the dome outline. The intrusive domes regarded in our previous studies have circularity values below 0.8, while the circularity is always higher than 0.9 for the effusive domes having flank slopes below 0.9° (Wöhler and Lena, 2009).

The circularity of the Aut1 dome of 0.99 should be attributed to an effusive construct. Regarding Aut1 as an effusive dome would imply to assign it to the effusive class C_1.

The rheologic model by Wilson and Head (2003) estimates the yield strength τ (the pressure or stress that must be exceeded for the lava to flow) and the plastic viscosity η, yielding a measure for the fluidity of the erupted lava, the effusion rate E (the lava

volume erupted per second) and the duration T of the effusion process. The computed values for τ, η, E, and T are valid for domes that formed from a single flow unit (monogenetic volcanoes). According to the model by Wilson and Head (2003), the viscosity of the dome-forming lava corresponds to $\eta = 1.2 \times 10^3$ Pa s. The lava erupted at high effusion rate of 2660 $m^3 s^{-1}$ over a period of time of 0.25 years (about 14 weeks). To estimate the magma rise speed and the feeder dike geometry, Wilson and Head (2003) apply the dike model by Rubin (1993). Dikes are rising vertical sheets of magma, which can reach the surface and erupt, forming a dome. Based on the estimated lava viscosity and effusion rate, this approach yields a magma rise speed of $U = 5.5 \times 10^{-2}$ m s^{-1}, a dike width of W = 3.3 m and a length of L = 15 km. These rheologic values were inferred assuming the minimum vertical magma pressure gradient of $dp/dz = 328$ Pa m^{-1} required to drive magma to the lunar surface as reported by Wilson and Head (1996). Wöhler et al. (2007) establish three rheologic groups of effusive lunar mare domes. The first group, R_1, is characterised by lava viscosities of 10^4–10^6 Pa s, magma rise speeds of 10^{-5}–10^{-3} m s^{-1}, dike widths around 10–30 m, and dike lengths between about 30 and 200 km. Rheologic group R_2 is characterised by low lava viscosities between 10^2 and 10^4 Pa s, fast magma ascent ($U > 10^{-3}$ m s^{-1}), narrow (W = 1–4 m) and short (L = 7–20 km) feeder dikes.

The third group, R_3, is made up of domes which formed from highly viscous lavas of 10^6–10^8 Pa s, ascending at very low speeds of 10^{-6}–10^{-5} m s^{-1} through broad dikes of several tens to 200 m width and 100–200 km length. According to the rheologic properties inferred for the dome Autolycus 1, it clearly belongs to rheologic group R_2 like several shallow domes in northern Mare Tranquillitatis.

References

[1] Burns, R. G., Parkin, K. M., Loeffler, B. M., Leung, I. S., & Abu-Eid, R. M., 1976. Further characterization of spectral features attributable to titanium on the moon. Lunar Science Conference 7, pp. 2561–2578.

[2] Charette, M. P., McCord, T. B., Pieters, C., & Adams, J. B., 1974. Application of remote spectral reflectance measurements to lunar geology classification and determination of titanium content of lunar soils. Journal of Geophysical Research, 79 (11), 1605–1613.

[3] Davies, M. E., Colvin, T. R., Meyer, D. L., & Nelson, S., 1994. The unified lunar

control network: 1994 version. Journal of Geophysical Research, 99 (E11), 23211–23214.

[4] Eliason, E., Isbell, C., Lee, E., Becker, T., Gaddis, L., McEwen, A., & Robinson, M., 1999. Mission to the Moon: the Clementine UVVIS global mosaic. PDS Volumes USA NASA PDS CL 4001 4078. http://pdsmaps.wr.usgs.gov

[5] Gillis-Davis, J. J., Lucey, P. G., & Hawke, B. R., 2006. Testing the relation between UV-vis color and TiO2 content of the lunar maria. Geochimica and Cosmochimica Acta, 70 (24), 6079–6102.

[6] Head, J. W., & Gifford, A., 1980. Lunar mare domes: classification and modes of origin. The Moon and Planets, 22, 235–257.

[7] Horn, B. K. P., 1989. Height and Gradient from Shading. MIT technical report 1105A.
http://people.csail.mit.edu/people/bkph/AIM/AIM-1105A-TEX.pdf

[8] Lena, R., Wöhler, C., Bregante, M . T., & Fattinnanzi, C., 2006. A combined morphometric and spectrophotometric study of the complex lunar volcanic region in the south of Petavius. Journal of the Royal Astronomical Society of Canada, 100 (1), 14–25.

[9] Lena, R., Wöhler, C., Lazzarotti, P., Phillips, J. 2011. Identification of a megadome near the lunar crater Kies: Morphometric analysis and proposed intrusive origin. Journal of the Royal Astronomical Society of Canada, vol. 105, no. 1, pp. 6-14.

[10] Lena, R., & Wöhler, C., 2008. Consolidated Lunar Dome Catalogue. http://digilander.libero.it/glrgroup/consolidatedlunardomecatalogue.htm

[11] Lucey, P. G., Blewett, D. T., & Hawke, B. R., 1998. Mapping the FeO and TiO_2 content of the lunar surface with multispectral imagery. Journal of Geophysical Research, 103 (E2), 3679–3699.

[12] Mosher, J., & Bondo, H., 2006. Lunar Terminator Visualization Tool (LTVT). http://inet.uni2.dk/ d120588/henrik/jim ltvt.html

[13] Rubin, A. S., 1993. Dikes vs. diapirs in viscoelastic rock. Earth and Planet. Sci. Lett. 199, pp. 641-659.

[14] Wilhelms, D. E., 1987. The geologic history of the Moon. USGS Professional Paper 1348.

[15] Wilson, L., Head, J. W., 1996. Lunar linear rilles as surface manifestations of dikes: theoretical considerations. Lunar Planet. Sci. XXVII, abstract #1445.

[16] Wilson, L., and Head, J. W., 2003. Lunar Gruithuisen and Mairan domes: Rheology and mode of emplacement. Journal of Geophysical Research, 108 (E2), 5012, doi:10.1029/2002JE001909.

[17] Wöhler, C., Lena, R., Lazzarotti, P., Phillips, J., Wirths, M., & Pujic, Z., 2006. A combined spectrophotometric and morphometric study of the lunar mare dome fields near Cauchy, Arago, Hortensius, and Milichius. Icarus, 183, 237–264.

[18] Wöhler, C., Lena, R., & Phillips, J., 2007. Formation of lunar mare domes along crustal fractures: Rheologic conditions, dimensions of feeder dikes, and the role of magma evolution. Icarus, 189 (2), 279–307.

[19] Wöhler, C., & Lena, R., 2009. Lunar intrusive domes: Morphometric analysis and laccolith modelling. Icarus, 204 (2), 381-398.

Wallace and the Domes of "*Mons Giraffe*"

by Federico G. Corno (ALPO & GLR Group)

Abstract

A description of a visual observation of two domes immediately south of Wallace is given: evidences collected in the drawings produced by the author are compared with images by Apollo, Clementine, LRO and Moon Geological Map.

1. Enviroment

In the south-eastern section of Mare Imbrium the stage was set to understand and establish the fundamental principles of lunar stratigraphy. The relationships between Copernicus, Eratosthenes, the lavas filling Mare Imbrium, Archimedes, the Apenninus bench and the Montes Apenninus demonstrated that events occurred in an ordinate sequence, here from youngest to oldest, as it may be derived from the reciprocal overlapping of the various structures.

In Figure 1 the south-eastern section of Mare Imbrium is shown in an image by Carmelo Zannelli, acquired during a GLR group survey of the examined region. The district herein discussed occupies the lowest left portion of the image, stretching south of the mostly degraded crater Wallace, just north of the Mons Wolf. The latter is part of the Montes Apenninus range, the most external ring of the Imbrium Basin. Between Wallace and the Montes Apenninus lies a short strip of low relieves, nicknamed in an unofficial way "*Mons Giraffe*" by the author, because vaguely resembling the head and neck of a giraffe in its easternmost part (see Figure 2).

The relief chain runs eastward from the vicinity of the twin craters Eratosthenes A and B up to the lone Wallace A (the "eye" of the *Giraffe*), in a direction parallel to the main mountain range. The relieves are embayed by Upper Imbrian lavas and sprinkled, as all the surroundings, with ray material from impacts forming Eratosthenes and Copernicus. In the area, both ridges and troughs are present.

2. Observation

The observation required to be split over two separated sessions: drawing is a time consuming technique, and stretching the observation over a period longer than 30-40 minutes may cause errors in picturing the shadows and determining hue density.

Figure 1: A panorama of the south-eastern quadrant of Mare Imbrium, from Archimedes to the Montes Apenninus. At the low left the highly ruined crater Wallace. South of it the district object of this article. Image courtesy by Carmelo Zannelli (from the GLR group archive).

Figure 2: Observation by the author taken on the night of the 11th of April 2011, starting from 20:30 UT. Telescope used was a 5" apochromatic refractor, operated at 260x. Craters Wallace A and K (WA and WK respectively) can be seen, while the discussion is focused on the elliptical dome D crossed by a series of relieves vaguely recalling the neck and head (at the far right) of a giraffe. Relieves to the left partially overlap with Figure 3.

Furthermore, low relief of the domes quickly makes them vanish as soon as the sun elevation increases.

The most peculiar features to observe in the area are two domes: figures 2 and 3 show them, emplaced in the eastern and westernmost sections respectively. The two figures overlap in the proximity of the ridge indicated with R in Fig. 3. The most complex of the two domes spreads on both sides of the relief chain, north and south of it (Fig. 2). Its shape is vaguely elliptical, with a major axis oriented N-S and close to 30 km in length.

Its surface is disturbed by numerous peaks clearly belonging to the Apennine system relieves. Finally, the slope is quite gentle, as it is confirmed by the need of low sun to easily spot it.

The second dome reported is smaller (Fig. 3), with a major axis closer to 20 km, oriented in the NNW-SSE direction. Under the present observing conditions, no features can be seen on its surface, but the presence of craterlets has been positively reported by both Earth based observers and space probes. Being them off-center, they have been described as originated by secondary impacts from larger craters in the district.

Craterlets poking all the region are easily detected in the UV-Vis image of the district by Clementine, unable to show neither of the domes (Figure 4), or have been observed during the Apollo flyby (Figure 5).

The slope of the second dome is even gentler than that the previous, and the edifice apparently lies on another very moderate relief, expanding as a subdued bulge to the east: it is displayed in the drawing as a shade of grey lighter than the mare material surrounding Eratosthenes A and B (see detail D' in Figure 3).

Such a feature is reasonably a section of the dome itself, difficult to recognize, but defined enough to change the actual dome shape to roundish rather than elliptical as initially perceived.

Slightly apart to the west of the dome runs a sinuous rille, not reported in the drawing (Near Side - LROC Image Browser, web site). Both domes are reported in Moon Geological Map I463, shown in Fig. 6, (Hackman, 1967): the first is embayed in an area larger than that recognized in the visual observation in Figure 2, while the D' portion of the second is apparently not reported, as it is not the rille.

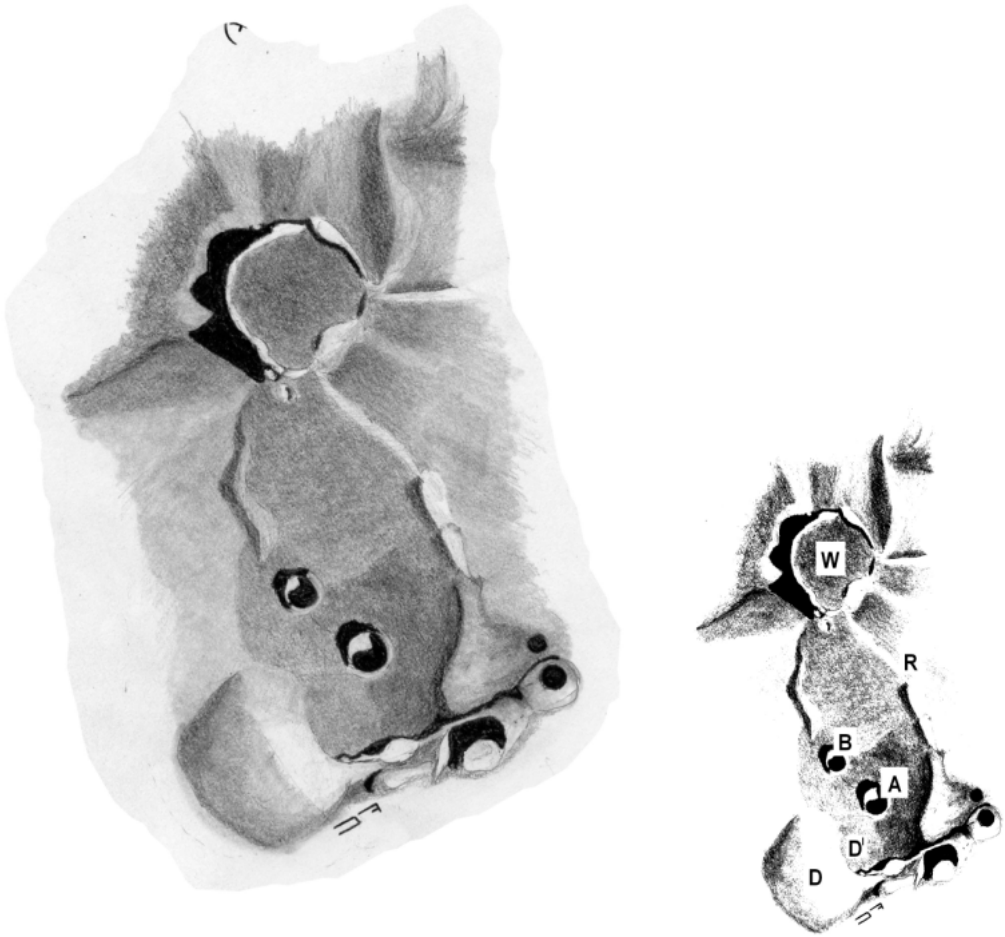

Figure 3: Observation by the author taken on the night of the 5th of October 2011, starting from 18:40 UT. Instrumentation as in Figure 2. Crater Wallace (W) lies to the north of twin craters Eratosthenes A and B (A and B). A ridge (R) runs from the crater southward to the "Mons Giraffe" westernmost reaches. A dome (D) is emplaced to the left, with a subdued portion expanding to the right (D'). Overlap with Figure 1 occurs close to the ridge R.

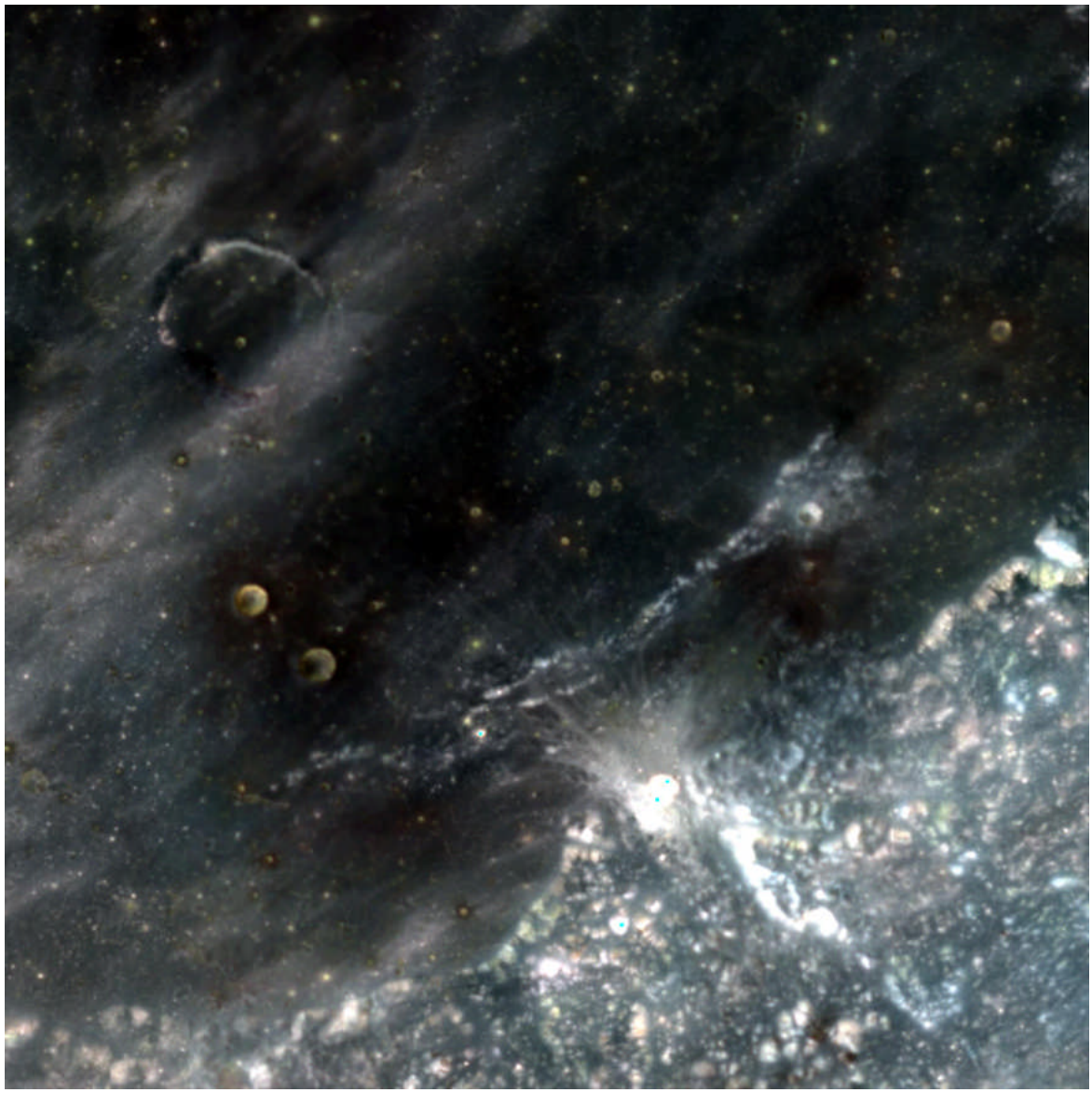

Figure 4: Clementine image (UV-Vis) ranging from 16 through 22° North and from 4 through 10° W. Note the numerous craterlets pocking the surface.

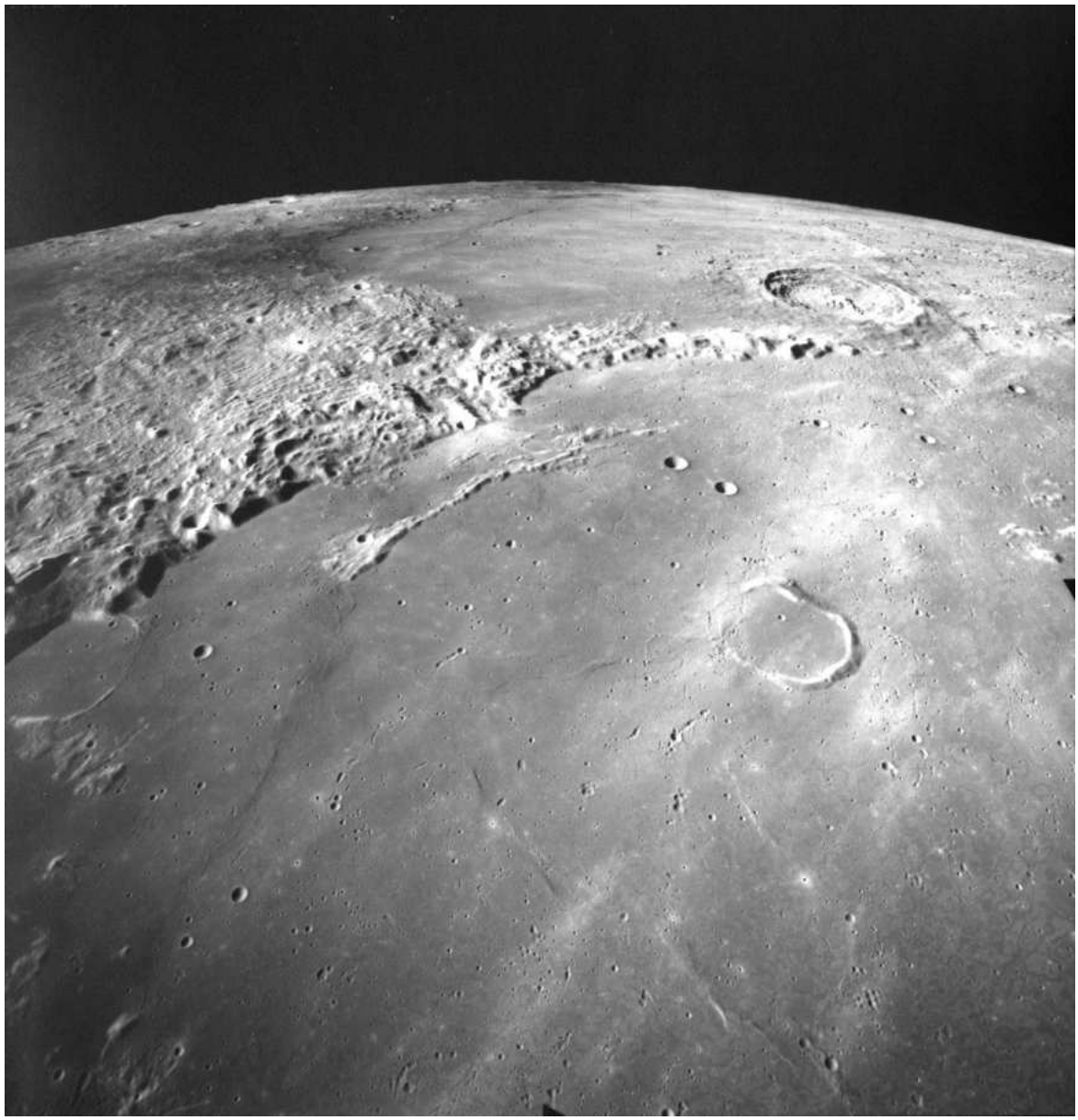

Figure 5: Apollo image AS17-M-2434, looking southward toward Wallace, in the center right: several craterlets are recognizable, but the first of the two domes can be barely glimpsed. The second stretches on the right of Eratosthenes A, but still is quite inconspicuous in this pictures.

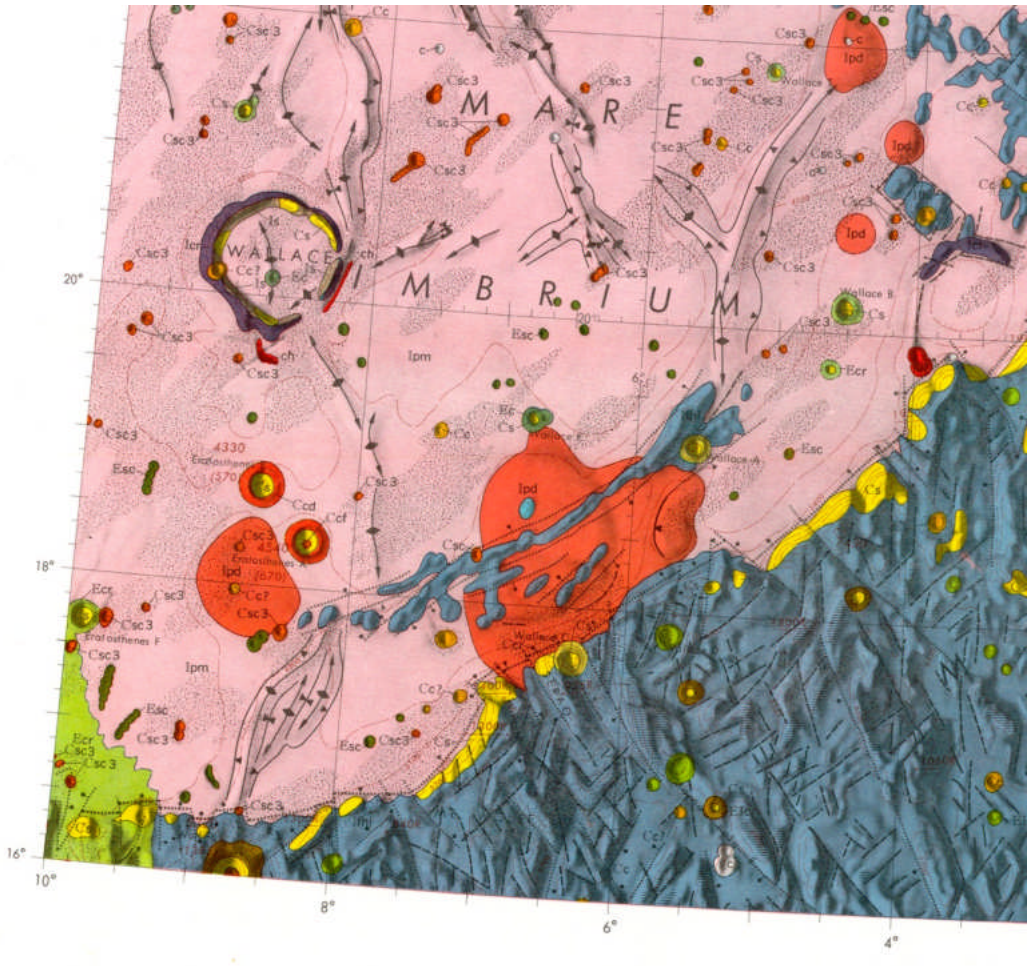

Figure 6: crop from Moon Geological Map I 463: orange hue indicates dome material, blue the Montes Apenninus, whose surface is here identified as a part of the Fra Mauro Formation (crushed rocks ejected from the Imbrium Basin blanketing the external ring of the basin). Note the extension of the first dome and the lack of the portion D' of the second. Ray material deposited from Eratosthenes and Copernicus impacts are represented as dotted areas.

3. Conclusion

In two visual observations two large domes have been described and depicted: their visibility is difficult if not under low sun, so a final definition of the actual size and shape is not easily achieved visually.

From an initial analysis, the lack of summit craters, their proportions and their elongated shapes suggest they are possible candidate intrusive domes as *laccoliths* (cf. Wöhler & Lena, 2009). The complexity of the two features and their relation with the environment make them a target deserving a systematic and quantitative future investigation by the Geological Lunar Research Group.

References

[1] Hackman, R. J. (1967). Geologic Map of the Montes Apenninus Region of the Moon I463.

[2] USGS. Near Side - LROC Image Browser, last accessed on 10-20, 2011 from LROC Image Browser: http://wms.lroc.asu.edu/lroc_browse/view/wac_nearside

[3] Wöhler, C., & Lena, R., 2009. Lunar intrusive domes: Morphometric analysis and laccolith modelling. Icarus, 204 (2), 381-398.

Detection of two probable meteoroidal impacts on the Moon

Marco Iten [(a)], Raffaello Lena [(b)], Stefano Sposetti [(c)]

(a) Garden Observatory

(b) Geologic Lunar Research (GLR) Group

(c) Gnosca Observatory

Abstract

In the course of our monitoring of the lunar surface of October 21 2011, we could detect 2 light flashes. These flashes were simultaneously detected by two telescopes and videocams placed 13km apart. Both flashes were quite brief. We can argue these flashes are probably meteoroidal impacts on the Moon. We can not say if these events are related with some major active meteor streams (i.e. orionids) or if these come from sporadic meteoroids. In addition the masses of the impactors are estimated using a nominal model with conversion efficiency from kinetic to optical energy of 2×10^{-3} and 2×10^{-2}. The results show that the meteoroids are likely to range in size from about 3 to 16 cm in diameter producing craters of about 3-8 m in diameter.

1. Instruments and observing methods

Our equipment and observing procedure was presented and discussed in preceding articles (Sposetti et al., 2011; Lena et al., 2011) published in Selenology Today.

We just summarize that we observe from two locations with three different telescopes: one instrument is a 125mm refractor and is located in Gordola, Switzerland. The other two instruments are a 280mm and a 420mm reflectors located in Gnosca, Switzerland. The two observatories are located at a distance of 13km. The instruments are equipped with Watec 902H2 Ultimate and Watec 902H2 Supreme videocameras. Three GPS time inserters (KIWI-OSD and IOTA-VTI) print the Universal Time with 1pps precision in the video frames. Time synchronicity of the various files is therefore assured. During the two events, no artificial satellites were in a 5° diameter field of view.

The selenographic coordinates were computed using the image shown in Figs. 1and 2, displaying several lunar features that were of very low contrast on the dark limb of the

imaged surface. After alignment with the edge of the lunar disk, computation of the libration and overlay of the rotated Moon's surface matching the imagery, a coordinate map was superimposed on the flash images. This procedure was performed using the LTVT software package by Mosher and Bondo (2006). The photometry was calculated using the star SAO 98102 (A0V, 8.71magV) inside the field of view at about 04:39UT. We performed the method of aperture photometry and used v.1.1.0.360 of Tangra© software by Hristo Pavlov (http://www.hristopavlov.net/Tangra).

2. The detections

Two impacts were simultaneously recorded by two observatories and are shown in Figures 1 and 2. Data are reported in Table 1 and 2. Figure 5 and 6 show the location on the Moon of the detected flashes with the potential impact Orionids region (© Lunarscan).

	Flash N. 1	Flash N. 2
Date	Oct 21 2011	Oct 21 2011
UTC Time (hh:mm:ss)	03:36:57.0	04:32:34.9
Duration (s)	0.08 ± 0.04	0.12 ± 0.02
Magnitude(V)	9.4 ± 0.5	8.5 ± 0.4
Selenographic Coordinates	Long 30 ± 3° E Lat 18 ± 3° N	Long 28° ± 3° E Lat: 37° ± 3°S
Remarks	near Fabbroni and Vitruvius	near Stiborius B-Riccius

Table 1.The two data flashes

	Flash N. 1	Flash N. 2
Moon Coordinates (Equatorial 2000.0)	RA: 08h 45m ; Dec: +13° 16'	RA: 08h 46m ; Dec: +13° 07'
Moon Horizon Coordinates	Az: 122° 24' ; Alt: +43° 32'	Az: 138° 55' ; Alt: +50° 32'
Phase (%)	39.46	39.05
Air Mass	1.45	1.30
Moon angular diameter	31' 34"	31' 35"
Moon distance (km)	378577	378346

Table 2. Moon Data (as seen from Sposetti's Gnosca Observatory)

3. Luminous efficiencies of the impactors and initial mass estimates

According to Ortiz et al. (2006) the masses of the impactors are estimated using a nominal model with conversion efficiency from kinetic to optical energy of 2×10^{-3} and 2×10^{-2}. The parameters used in the calculation are the projectile density (2000 kg m^{-3}), the target density (2000 kg m^{-3}) and the impact velocity. Using the luminous efficiency $\eta = 2 \times 10^{-3}$ (the nominal value determined from Leonid impact flashes, e.g., Bellot Rubio et al., 2000; Ortiz et al., 2002) and the typical speed of the orionids (67 km s^{-1}), the masses of the impactors would be 0.074 kg and 0.250 kg for Flash 1 and 2, respectively. Based on the above data and assuming a spherical projectile, the diameter of the impactors were inferred to be approximately of about 4-6 cm.

A luminous efficiency of 2×10^{-2} yields a mass of the impactors considerably less than the preceding inferred values by a factor of 10. Using Gault's scaling law in regolith for crater sizes (Melosh, 1989; Melosh and Beyer, 1999), the size of the lunar impact craters were computed to be about 3-5 m. We have assumed also that the impacts come from sporadic meteoroids. According to the statistics of a large meteoroid orbit database (Steel, 1996) the speed for sporadic meteoroid is approximately 20.2 km s^{-1} on Earth and 16.9 km s^{-1} on the Moon, after correcting for the different escape velocities of the Earth and the Moon. Using the luminous efficiency $\eta = 2 \times 10^{-3}$ the masses of the impactors would be 1.1 kg and 3.9 kg for Flash 1 and 2, respectively. For sporadic impact flashes on the Moon a luminous efficiency of 2×10^{-2} yields a mass of the impactors considerably less than the preceding inferred values by a factor of 10.

In this case, assuming the same parameters as those used in the previous computations, the impact flashes appear to have been produced by a body with diameters of approximately 5 and 8 cm, respectively, when assuming a spherical projectile. Using Gault's scaling law the size of the lunar impact craters were computed to be 3-5 m for $\eta = 2 \times 10^{-2}$ and about 5-8 m for $\eta = 2 \times 10^{-3}$. It should be noted, however, that these values are "nominal", since the results includes uncertainties in the projectile density, meteoroid mass, luminous efficiency and identification of meteor streams (i.e. orionids) or if these come from sporadic meteoroids.

Based on a modelling analysis of both cases, the meteoroids are likely to range in size from about 3 to 16 cm in diameters and produced craters of about 3-8 m in diameter.

Fig. 1. Field images of the flash N.1

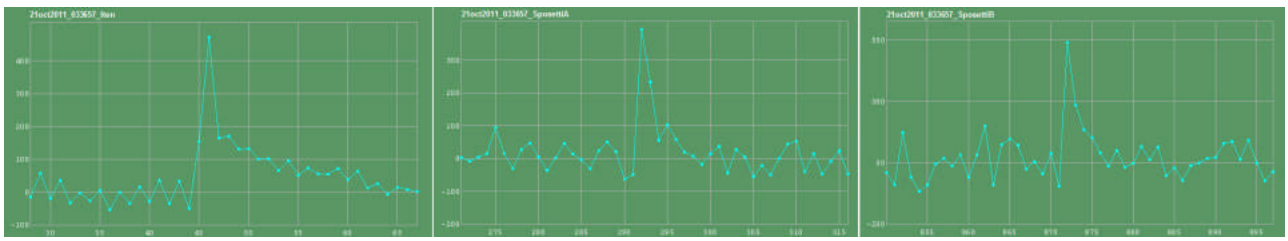

Fig. 2. Lightcurves of the flash N.1. Time interval is 0.020s

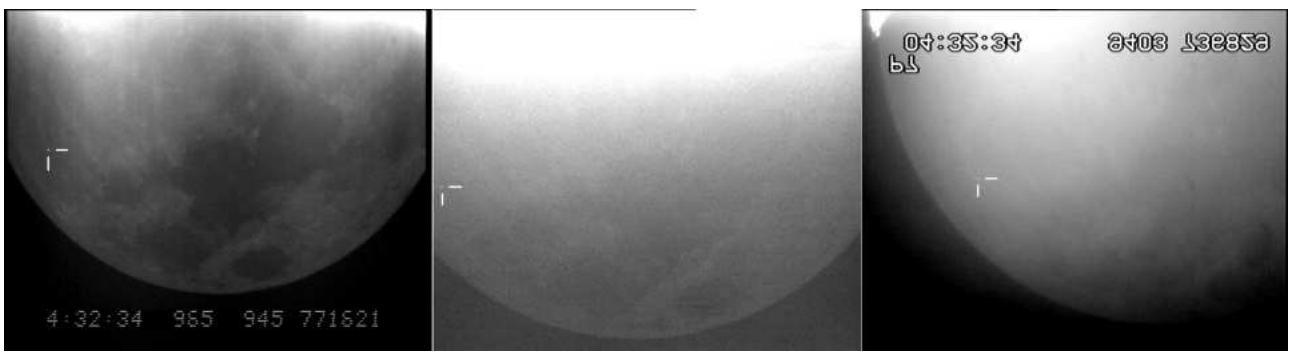

Fig. 3. Field images of the flash N.2

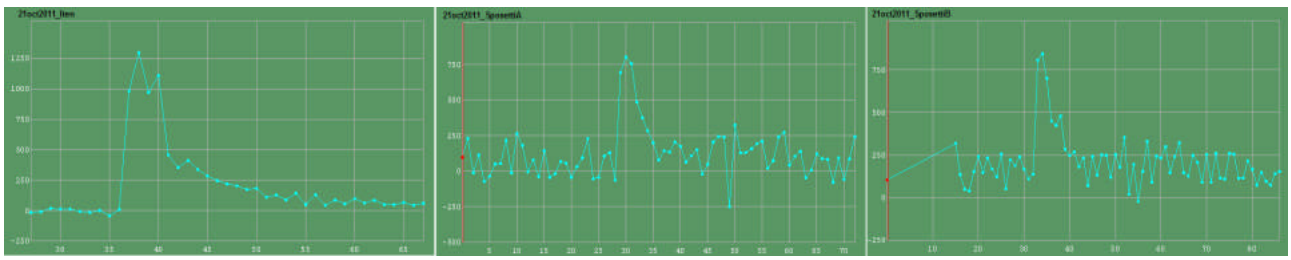

Fig. 4. Lightcurves of the flash N.2. Time interval is 0.020s

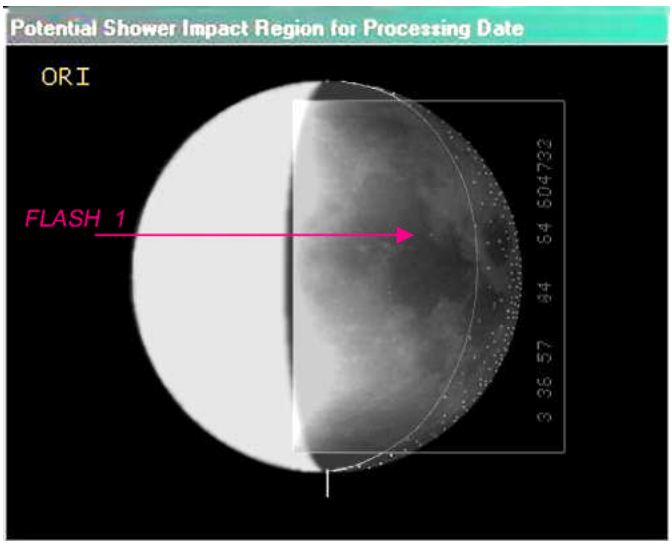

Fig. 5. Location on the Moon of the flash N.1 with the potential impact Orionids region (© Lunarscan).

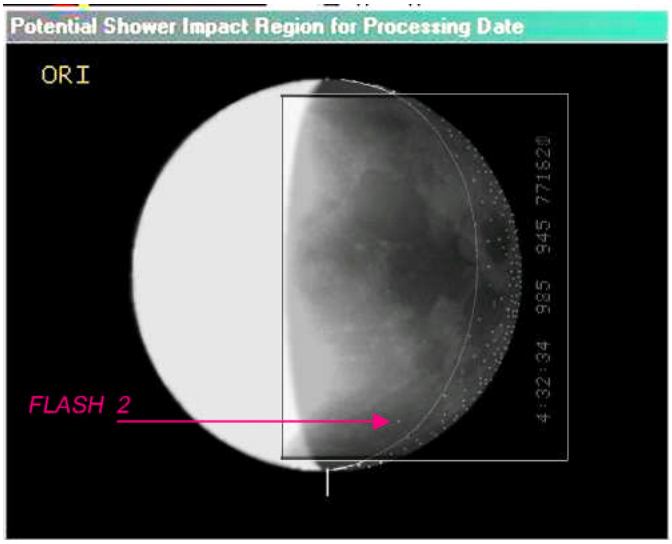

Fig. 6. Location on the Moon of the flash N.2 with the potential impact Orionids region (© Lunarscan).

References

[1] Bellot Rubio, L.R., Ortiz, J.L., Sada, P.V., 2000. Observation and interpretation of meteoroid impact flashes on the Moon. Earth Moon Planets 82–83, 575–598.

[2] Lena, R., Iten, M., Sposetti, S., 2011. Detection of three meteoroidal impact on the Moon. Selenology Today 24, 12-29.

http://digidownload.libero.it/glrgroup/selenologytoday24.pdf

[3] Melosh, H.J., 1989. Impact Cratering: A Geologic Process. Oxford Univ. Press, New York.

[4] Melosh, H.J., and Beyer, R. A. 1999. Computing Crater Size from Projectile Diameter. http://www.lpl.arizona.edu/tekton/crater.html

[5] Mosher, J., & Bondo, H., 2006. Lunar Terminator Visualization Tool (LTVT).

http://inet.uni2.dk/ d120588/henrik/jim ltvt.html

[6] Ortiz, J.L., Aceituno, F.J., Quesada, J.A., Aceituno, J., Fernández, M., Santos-Sanz, P., Trigo-Rodríguez, J.M., Llorca, J., Martín-Torres, F.J., Montañés-Rodríguez, P., Pallé E. 2006. Detection of sporadic impact flashes on the moon: Implications for the luminous efficiency of hypervelocity impacts and derived terrestrial impact rates. Icarus 184. 319-326.

[7] Ortiz, J.L., Quesada, J.A., Aceituno, J., Aceituno, FJ., Bellot Rubio, L.R. 2002. Observation and interpretation of Leonid impact flashes on the Moon in 2001. Astrophys. J. 576. 567–573.

[8] Sposetti, S., Iten, M., Lena, R. 2011. Detection of a meteoroidal impact on the Moon. Selenology Today 23, 1-32.

http://digidownload.libero.it/glrgroup/selenologytoday23.pdf

[9] Steel, D., 1996. Meteoroid orbits. Space Sci. Rev. 78, 507–553.